2017

The Impact of Quantum Size Effects on Thermoelectric Performance in Semiconductor Nanostructures

Adithya Kommini
University of Massachusetts Amherst

THE IMPACT OF QUANTUM SIZE EFFECTS ON THERMOELECTRIC PERFORMANCE IN SEMICONDUCTOR NANOSTRUCTURES

A Thesis Presented

by

ADITHYA KOMMINI

THE IMPACT OF QUANTUM SIZE EFFECTS ON THERMOELECTRIC PERFORMANCE IN SEMICONDUCTOR NANOSTRUCTURES

A Thesis Presented

by

ADITHYA KOMMINI

Approved as to style and content by:

_____

Zlatan Aksamija, Chair

_____

Eric Polizzi, Member

_____

C Andras Moritz, Member

_____

Christopher V. Hollot, Department Head
Electrical and Computer Engineering

DEDICATION

To my family.

ACKNOWLEDGMENTS

I would be ever grateful to my advisor, Prof. Zlatan Aksamija, for his thoughtful, patient guidance and support. Special thanks to Prof. Eric Polizzi and Prof C. Andras Moritz, for kindly serving as my thesis committee and providing valuable suggestions that improved the quality of this study.

I wish to thank my family without whom none of this would ever have been possible. I have had their love and support in everything I have done. Thank you.

A special thank you to all those whose support and friendship helped me to stay focused on completing the thesis and who have provided me with the encouragement to continue when the going got tough.

ABSTRACT

THE IMPACT OF QUANTUM SIZE EFFECTS ON THERMOELECTRIC PERFORMANCE IN SEMICONDUCTOR NANOSTRUCTURES

FEBRUARY 2017

ADITHYA KOMMINI

B.Tech., JNT UNIVERSITY, ANANTAPUR

M.S.E.C.E., UNIVERSITY OF MASSACHUSETTS AMHERST

Directed by: Professor Zlatan Aksamija

An increasing need for effective thermal sensors, together with dwindling energy resources, have created renewed interests in thermoelectric (TE), or solid-state, energy conversion and refrigeration using semiconductor-based nanostructures. Effective control of electron and phonon transport due to confinement, interface, and quantum effects has made nanostructures a good way to achieve more efficient thermoelectric energy conversion. This thesis studies the two well-known approaches: confinement and energy filtering, and implements improvements to achieve higher thermoelectric performance. The effect of confinement is evaluated using a 2D material with a gate and utilizing the features in the density of states. In addition to that, a novel controlled scattering approach is taken to enhance the device thermoelectric properties. The shift in the onset of scattering due to controlled scattering with respect to sharp features in the density of states creates a window shape for transport integral. Along with the controlled scattering, an effective utilization of Fermi

window can provide a considerable enhancement in thermoelectric performance. The conclusion from the results helps in selection of materials to achieve such enhanced thermoelectric performance. In addition to that, the electron filtering approach is studied using the Wigner approach for treating the carrier-potential interactions, coupled with Boltzmann transport equation which is solved using Rode's iterative method, especially in periodic potential structures. This study shows the effect of rapid potential variations in materials as seen in superlattices and the parameters that have significant contribution towards the thermoelectric performance. Parameters such as period length, height and smoothness of such periodic potentials are studied and their effect on thermoelectric performance is discussed. A combination of the above two methods can help in understanding the effect of confinement and key requirements in designing a nanostructured thermoelectric device that has a enhanced performance.

TABLE OF CONTENTS

LIST OF FIGURES

CHAPTER 1

INTRODUCTION

1.1 Overview

Global demand for cost-effective, environmentally friendly forms of energy conversion inspired people to focus on the field of thermoelectrics. To meet the ever increasing demand for power sources, there is a need to improve our energy sources. Renewable energy sources can be used as an alternative to the non-renewable energy sources, but their efficiency and production capabilities aren't able to satisfy the increasing demand. Besides this, there is a possibility to effectively utilize the current generation methods using coal and nuclear energy, but a lot of energy is going waste in the form of heat dissipation in these methods. This can be used to produce electricity but it requires reliable and efficient thermoelectric devices. Besides that, an increasing need for effective thermal sensors have created renewed interests in thermoelectric (TE), or solid-state, energy conversion and refrigeration. The efficiency of thermo-electric devices for power generation is determined by dimensionless Figure-of-merit (ZT) of material [17]:

$$ZT = \frac{\sigma S^2}{\kappa_e + \kappa_p} T \tag{1.1}$$

where σ is electrical conductivity, S is Seebeck coefficient, κ_e is electronic thermal conductivity, κ_p is lattice (phonon) thermal conductivity. In Eq. 1.1, ZT is related to S, κ_e, σ, which depend on electronic structure of materials and κ_p depends on lattice. In the quest for efficient thermoelectric device/material, a lot of materials has been investigated and studied.

1.2 Physics behind the Thermoelectric energy conversion

Energy and particle transport accompany each other in a material, especially in thermoelectrics where the temperature difference is maintained between the ends. Let us consider a basic p-type and n-type semiconductor which are connected at ends that are maintained at different temperatures as shown in Fig. 1.1. The electrons
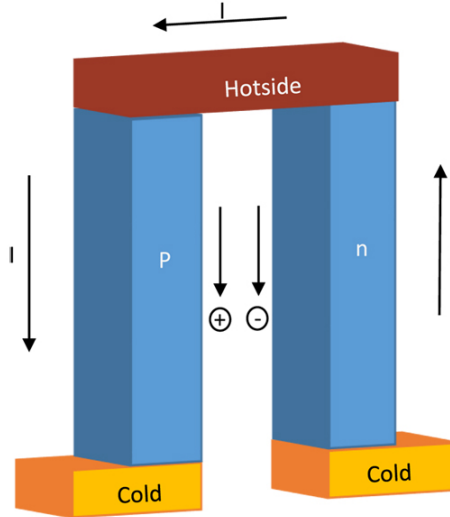
Figure 1.1: A thermoelectric device with p-type and n-type semiconductor legs.

and holes diffuse from hot side to cold side to distribute the energy that is supplied to the hot side. This energy transfer creates a cooling effect called Peltier cooling at the hot junction and a heating effect at the cold junction. This carrier diffusion creates a potential difference between the two junctions. This process of creating a potential difference (ΔV) between two junctions at different temperatures (ΔT) is called as Seebeck effect. The energy transport that gives rise to heating and cooling trends are governed by Peltier coefficient (Π) and the potential difference between the junctions is gauzed by Seebeck Coefficient (S) where

$$S = -\Delta V / \Delta T \tag{1.2}$$

Peltier coefficient (Π) and Seebeck Coefficient (S) are related using the kelvin relation which is given as.

$$\Pi = ST \tag{1.3}$$

A number of such p-type and n-type are connected such that they are thermally parallel and electrically in series to create a thermoelectric device. But still, there is no economical thermoelectric device that can be used for electrical generation in large scale using Seebeck effect instead of conventional energy generation methods. Fig. 1.1 shows the comparison between the efficiency of thermoelectrics that has to be achieved to the efficiencies of conventional energy sources.
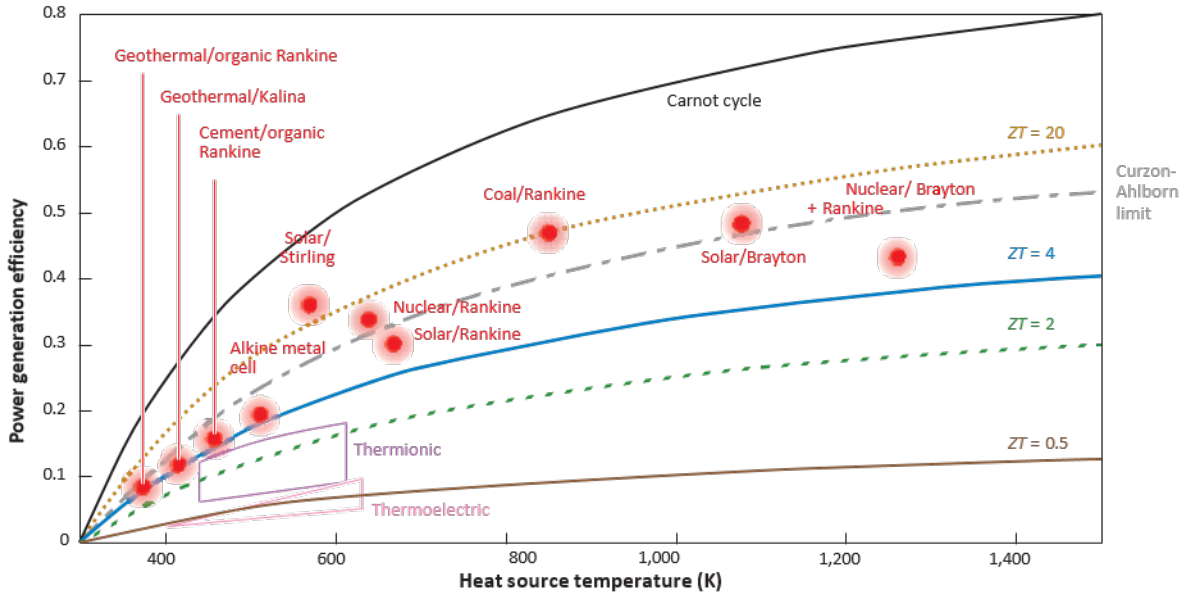
Figure 1.2: Comparison of thermoelectric power generation efficiency versus efciency for conventional mechanical engines as well as the Carnot limit taken from [44].

Even though ZT is a measure of thermoelectric energy conversion, the power factor σS^2, which is a part of ZT is mostly used to compare the efficiency of different materials and devices. In metals, electrical conductivity σ is high but has a low Seebeck coefficient. In insulators, the electrical conductivity is less but high Seebeck coefficient. But, semiconductors have a moderate electrical conductivity and Seebeck

coefficient that give a good power factor compared to the insulators and metals making them the suitable materials for thermoelectrics. Even though the total thermal conductivity (κ) of semiconductors can be reduced without causing much change in electrical conductivity, as phonons contribute more to thermal conductivity than electrons. The phonon thermal conductivity (κ_p) depends on the lattice of the material and can be reduced by using different approaches like edge roughness and interface scattering [9, 31, 45] such as isotope insertion [32], grain boundaries [48, 4], and boundary confinement [1, 3] without significantly changing the transport properties of electrons. These changes can modify the phonon thermal conductivity as they change the relaxation time of the phonons due to different scattering processes that are being introduced. Besides this, a lot of effort is made to enhance the power factor by changing the electronic band structure. This thesis is an effort to improve the thermoelectric performance by changing the electronic band structure using quantum size effects like confinement and periodic structures.

1.3 Outline of Thesis

This Thesis is organized as follows: Chapter 2 discusses the ways that have been reported in the literature to enhance thermoelectric performance using quantum size effects. Chapter 3 introduces the idea of improving Seebeck coefficient in a 2-D material using the density of states and restricting scattering of carriers. The numerical simulation results are shown implementing the idea. The effect of periodic structures is studied in chapter 4 by incorporating the carrier potential interactions using Wigner approach and results are reported. Conclusions are drawn in chapter 5.

CHAPTER 2

OVERVIEW ON ENHANCEMENT IN THERMOELECTRIC PERFORMANCE

2.1 Low-Dimensional Thermoelectric Structures

Seminal early work by Hicks and Dresselhaus [20] reported the possibility of improved ZT when moving from higher to lower dimensional materials using the change in the shape of density-of-states (DOS). They concluded that the sharp features in reduced-dimensional materials provide energy filtering and push the carrier energies upward (Since $S \propto (E - E_f)$)relative to their bulk counterparts, resulting in enhanced thermopower. There has been enormous research and innovations in the field over years mainly on nanostructured materials and devices. The two main approaches researched are using the nanostructuring or low-dimensional materials and hot electron filtering using thermionic emission. Some of them that have been reported in the literature for improving power factor are discussed below:

2.1.1 Quantum Wells

As discussed above the nanoscale effects like the sharp density of states can improve power factor, thereby the total efficiency. But, these nanoscale effects when implemented in devices and structures the resulting device thermoelectric efficiency is not as expected. The work by Hicks and Dresselhaus [19] predicted that the quantum confinement of carriers by using quantum wells increase ZT by increasing the density of states without affecting the electronic transport properties. This inspired people to work on quantum wells, but there are some fall-backs in implementing these changes. To impose quantum confinement, one has to create barriers, these barriers

result in heat loss from hot to cold terminals. If the barriers are made thin, then tunneling may broaden the energy levels and sharp features in the density of states may vanish. The size non-uniformity in materials and interface scattering in narrow quantum structures also affect the density of states, limiting the efficiency enhancement that can be achieved.

2.1.2 Quantum Wires

Quantum wires provide more quantum confinement than quantum wells. There are many theoretical studies showing a huge improvement in ZT due additional confinement. But there were no experimental results that indicate the same. Papers by Boukai [8] et al. and Hochbaum [21] et al. claimed a ZT of 0.6 for Silicon nanowires. There are reports showing that the boundary scattering in thin nanowires reduces thermal conductivity that improves ZT at low temperature. They also reported an improvement in ZT at low temperatures and attributed it to the phonon drag effects. Ryu et al. [43] also reported an increase in the contribution of phonon drag towards the thermoelectric efficiency at low temperatures. This phonon drag increases the Seebeck coefficient by using a phonon mode in electron transport that doesn't contribute much to thermal conductivity.

2.1.3 Quantum Dots

Quantum dots have zero dimension which provides high levels of quantum confinement. This gives a sharp density of states required to achieve high power factor. A single quantum dot doesn't help in making a thermoelectric device. It requires an array of quantum dots to form a thermoelectric device. The transfer of heat from one location to other require the movement of the electrons which is restricted if the energy barrier is narrow and carriers are highly confined. If the barrier is shallow then the sharp density of states is lost. When 3D array of dots is formed, then they behave like a bulk crystal. In their work Linke et al. [33] studied the coupling

between quantum dot energy level and reservoirs broadens the density of states and reduces the efficiency of the thermoelectric conversion process.

2.2 Thermionic Energy Conversion

To enhance the thermoelectric efficiency another approach called hot electron filtering can also be used. In this method potential barriers are introduced in the material to allow only high energy electrons to participate in the transport, thereby improving the Seebeck coefficient. These heterostructures can have single and multibarrier structures. In single barrier devices, an optimum height barrier is used in one direction and a large barrier is used in other direction to prevent the reverse current. In multibarrier barrier devices, Mahan and Woods [29] suggested an improvement by a factor by two but later concluded that it worse than the normal devices. Seebeck enhancement by hot electron filtering is observed in some systems [52], but this comes with a decrease in electrical conductivity because of reduced number of carriers.

The general interpretation of the carrier transport over the barriers is that the electron with higher kinetic energy perpendicular to the barrier is emitted. Many hot electrons with higher transverse momentum can't pass the barrier. To break this, non-planar barriers or scattering centers are created [7]. Moreover, the effect of barriers on the distribution function of the particles is not considered. If the non-planar or the scattering centers have a characteristic length less than electron de-Broglie wavelength, then wave nature of the electron has to be considered which makes the problem complex to analyze.

2.3 Calculation of Thermoelectric Performance Parameters

To evaluate the efficiency of thermoelectrics, Figure-of-merit (ZT)(Eq. 1.1) is the commonly used parameter. Calculation of ZT requires the calculation of Seebeck coefficient (S), electrical conductivity (σ) and Thermal conductivity of both electrons

(κ_e) and phonons (κ_p). This thesis deals only with the electron transport, so only Seebeck coefficient (S), electrical conductivity (σ) and Thermal conductivity of electrons (κ_e) is focused. To calculate them, Boltzmann Transport equation (BTE) with relaxation time approximation is used and additional effects to include the quantum treatment of electrons is added in later part of the thesis. Carrier transport occurs when the system is in a nonequilibrium state and to describe this nonequilibrium condition Boltzmann equation is used. Boltzmann equation is a one-particle distribution function by averaging the N-particle distribution function over ($N - 1$) particles in the system. This averaging process gives the Boltzmann equation as

$$\frac{\partial f}{\partial t} + v.\nabla_r f + \frac{F}{\hbar}.\nabla_k f = \left(\frac{\partial f}{\partial t}\right)_c \tag{2.1}$$

where f_q is the particle density. The right hand side (scattering or collision term) of the equation represents the interaction of this one particle with the rest of the particles in the system and calculates the change in particle density due to interaction with other particles. This term is influenced by two factors, diffusion and scattering. Diffusion is a result of the temperature gradient where as scattering is due to impurities, dislocations, grain boundaries, the collision between the phonons, between phonons and boundaries, and phonons with other particles. To calculate the collision term in the Boltzmann transport equation, Fermi golden rule was used which gives rate of transition of a particle from one set of quantum states to other. By integrating the transition of a particle at a particular quantum state into all possible quantum states gives the scattering term for that particle. Due to the complexity of the equation a simplification called Relaxation Time Approximation (RTA) for this term was used.

$$\left(\frac{\partial f}{\partial t}\right)_c = -\frac{f - f_0}{\tau} \tag{2.2}$$

Where τ represents the total relaxation time calculated from different processes which are later combined using Matthiessen's and f_0 represents the equilibrium distribution of the carriers. Then the expressions for S,σ and κ_e are derived under the assumption that the local deviation from equilibrium is small and the relation between heat transport and carrier transport is included using the first law of thermodynamics. The expressions thus calculated are:

$$\sigma = L^{(0)} \tag{2.3}$$

$$S = \frac{1}{eT}\frac{L^{(1)}}{L^{(0)}} \tag{2.4}$$

$$\kappa_e = \frac{1}{e^2T}\left(L^{(2)} - \frac{\left(L^{(1)}\right)^2}{L^{(0)}}\right) \tag{2.5}$$

$$L^{(\alpha)} = \int_0^\infty -\frac{\partial f_0\left(E\right)}{\partial E}(E - E_F)^\alpha \Xi(E)dE \tag{2.6}$$

$$\Xi(E) = e^2\tau(E)g(E)v^2(E) \tag{2.7}$$

where $L^{(\alpha)}$ is called transport integral, $\Xi(E)$ is called differential conductivity or Transport Distribution Function (TDF), E_F is called Fermi energy, E is energy of the carriers, $g\left(E\right)$ is density of states, $\tau\left(E\right)$ is energy dependent relaxation time, $\partial f_0\left(E\right)/\partial E$ is Fermi window factor and $v(E)$ is velocity of the carriers in the direction of the electric field or temperature gradient.

2.4 Trade-off between Electrical Conductivity and Seebeck coefficient

As discussed earlier, to improve power factor, both Seebeck and electrical conductivity has to be improved. But, improving one of them results in the decrease of the other so a balance has to be maintained to maximize both in a material. The differential electrical conductivity function or Transport distribution function (TDF) can

be used to study the trade-off between electrical conductivity and Seebeck coefficient. Now, the carefully observing the expression for Seebeck coefficient, it can be interpreted as the weighted average of energies above the Fermi level. To improve it the a matching peak in TDF with the peak in Fermi window $(\partial f_0\,(E)/\partial E)$ which occurs at Fermi energy. But this alone is not sufficient because a perfect symmetric function centered at Fermi level has a minimum contribution towards Seebeck coefficient. So the peaks have to be matched by keeping the overlap asymmetric with respect to Fermi energy. So using the low-dimensional materials which have sharp features in the density of states will help to improve the Seebeck coefficient and Electric conductivity simultaneously due to the asymmetry caused by those sharp features between the TDF and Fermi window. Doping can improve electrical conductivity by moving the Fermi energy well into the conduction band, thereby improving the electrical conductivity, but decreases the Seebeck coefficient due to the symmetry.

The electron group velocity which depends on the effective mass as $v(E) = \sqrt{\frac{2E}{m_v}}$ also causes trade-off between electrical conductivity and Seebeck coefficient especially in superlattices [6]. The bands having high effective mass results in the higher density of states and lower mobilities, resulting in high power factor. This is not the only possibility: even bands with high mobility and low effective mass also have good power factor as velocity depends only on the curvature of the bands whereas the density of states depends on the entire dispersion relation. So, selecting and implementing a good band structure can overcome this and a better power factor can be achieved with optimal electrical conductivity and Seebeck coefficient.

CHAPTER 3

ENHANCEMENT IN A GATED 2-D MATERIAL USING FEATURES IN DENSITY OF STATES

The initial work on improving the thermoelectric properties of materials suggests moving from higher to lower dimensional material [20] and tuning the TDF [28] to make it a delta shaped function helps to achieve higher conversion efficiency. Thermoelectric refrigeration using Si-based nanowires and nanoribbons is an attractive approach for targeted cooling of local hotspots [30],[11] due to the ease of on-chip integration and the nanowires' enhanced TE Figure-of-merit [21, 8]. Silicon-on-insulator (SOI) membranes [22] and membrane-based nanowires [39] and ribbons [8] show promise for application as efficient thermoelectrics, which requires both high power factor and low thermal conductivity.

3.1 Overview of our approach

Mahan and Sofo [28] studied the optimal conditions for thermoelectric conversion and proposed that a delta-shaped transport distribution function (TDF) $\Xi(E) = \tau(E)g(E)v^2(E)$, where $\tau(E)$ represents the relaxation time, $g(E)$ represents the DOS, and $v(E)$ is velocity of carriers, can significantly improve S thereby improving the overall ZT through electron filtering. Zhou et. al. [50] re-investigated this idea to determine the best electronic structure for materials in terms of energy filtering bandwidth (W_α) by studying the transport properties using different scattering models of carriers. They concluded that a narrow window-shaped, rather than a delta-function shaped TDF, brings about the highest enhancement in the TE properties, especially

when that window matches the so-called Fermi window [24]. Achieving a narrow or delta-shaped TDF, however, has proven difficult as the sharp features in the density-of-states $g(E)$ are readily canceled by related features in the scattering rate $\tau^{-1}(E)$.

In this work, we propose a novel method of further enhancing the thermoelectric Seebeck coefficient beyond what is achievable by confinement and reduced dimensionality alone. We study ways to achieve significant enhancement of Seebeck coefficient arising from narrow window-function shaped TDF. We propose to achieve this narrow TDF by combining a step-like DOS in a 2-dimensional system with predominantly inelastic scattering from the optical phonon emission mechanism. The narrow-band TDF is achieved due to electron confinement in a gated two-dimensional (2D) silicon nanomembrane (SiNR). The 2D nature of the system leads to a step-like electronic DOS $g_n^b(E) = m_n^b/(\pi\hbar^2)\Theta(E - E_n^b)$ with one step contributed by each subband n in each ladder b [5]. Typically, elastic scattering rates $\tau_{el.}^{-1}(E)$ are proportional to the DOS as they do not involve energy transfer; consequently, the number of possible transitions is closely related to the number of available final states, which is captured by the DOS. Because of this, sharp features in the DOS are canceled out by the equal and opposite features in the $\tau_{el.}$, which makes it difficult to achieve a delta-shaped TDF, even when the DOS has very sharp features. In addition, scattering tends to smear out the sharp features in the DOS due to collisional broadening.

In contrast, inelastic and intersubband scattering can only begin to occur when the carrier accumulates enough energy above the bottom of a band, or, in the case of confined structures, a subband. Consequently, inelastic scattering rates still follow the shape of the DOS, but they are shifted by the amount of energy being exchanged in the scattering event: $\tau_{inel.}^{-1}(E) \propto g(E \pm \Delta E)$, where ΔE is the energy being exchanged–either the difference in subband energies for intersubband scattering or the optical phonon energy $\hbar\omega_{op}$ for optical transitions. The subband energies can be controlled by gate-tuning thereby limiting the scattering of the carriers. Hence these mechanisms,
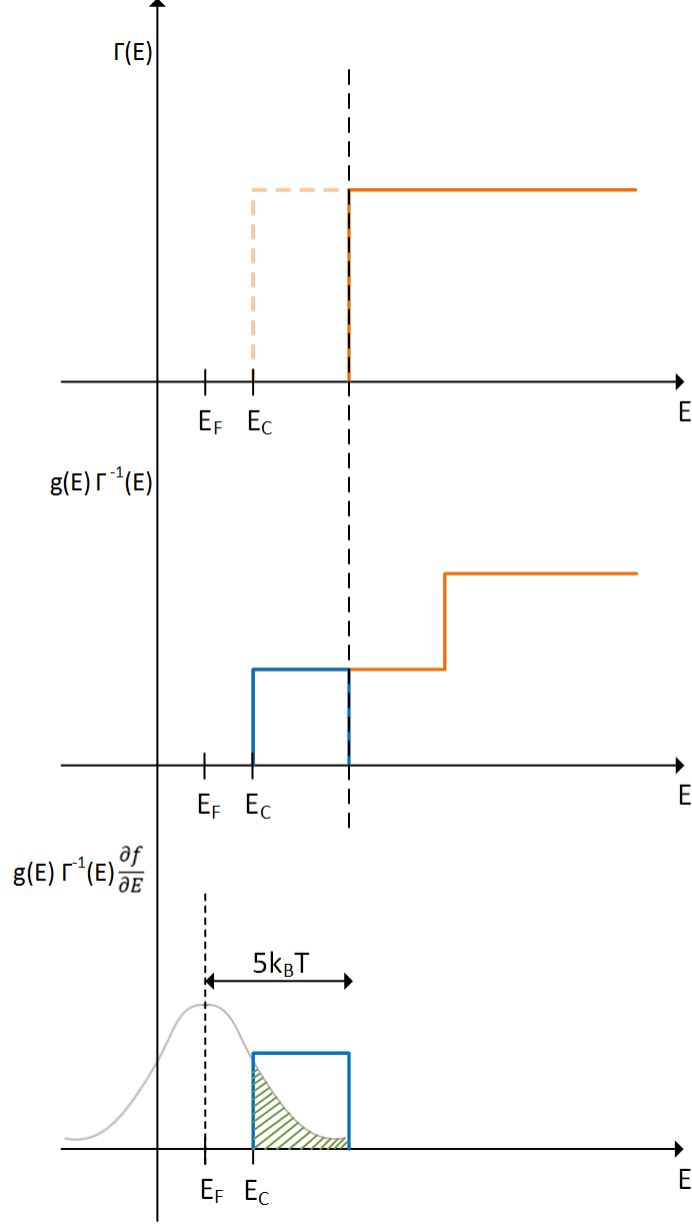
Figure 3.1: Schematic of the approach we proposed in this study. A shift in the onset of scattering rates (in top row) which respect to Density of states can give the proposed delta shape to TDF [27] (shown in the second row). Along with delta shaped TDF, maximum utilization of Fermi window still maintaining the asymmetry with respect to TDF (shown in the bottom figure) can provide maximum thermoelectric performance.

when inelastic scattering is dominant, delay the onset of the step in the scattering rate relative to the DOS. In this case, unlike its elastic counterpart, the DOS and

$\tau_{inel.}$ are offset by ΔE and thus lead to a narrow band TDF. This, along with the maximum utilization of the Fermi window, as shown in Fig. 3.1 lead to a significant further enhancement of the Seebeck coefficient at low temperatures where inelastic scattering due to optical phonon emission is dominant.

3.2 Transport Model

To explore the practical possibility of achieving the delta shaped TDF in a confined nanostructure, a back gated undoped silicon nanoribbon of 20 nm thickness on an oxide of 10 nm thickness is simulated. The oxide acts as a capacitor which induces carriers that participate in the transport of both charge and energy, by applying the bias to the gate. The subband energies in the nanoribbon are obtained by self-consistently solving the coupled one-dimensional Schrödinger and Poisson equations in the direction of confinement [2]. The 1D Poisson equation is solved for the potential over the entire simulation domain, including the gate contact, the buried oxide, the silicon nanoribbon, and the vacuum on the opposite side. The 1D Poisson problem

$$\frac{d^2 V(z)}{dz^2} = \frac{\rho(z)}{\epsilon(z)} \tag{3.1}$$

produces a tridiagonal system of equations $\sum_j A_{i,j} z_j = \rho(z_i)/\epsilon(z_i)$ when discretized by finite differences, and can then be solved very efficiently by the popular and robust Thomas algorithm which consists of one forward substitution pass followed by a back-substitution sweep, effectively eliminating the off-diagonal entries and diagonalizing the system matrix . The solution of the Poisson problem produces the values of the electrostatic potential $V(z)$ at each point in the discretization. Then the values of those points which are inside the silicon nanoribbon region ($0 \leq z \leq 20$ nm) are extracted from the total solution for the whole system. A few points (typically 5) are added on the SiO_2 side for $z < 0$ in order to account for penetration of the wavefunction into the oxide due to its finite barrier height. A potential barrier is added to the
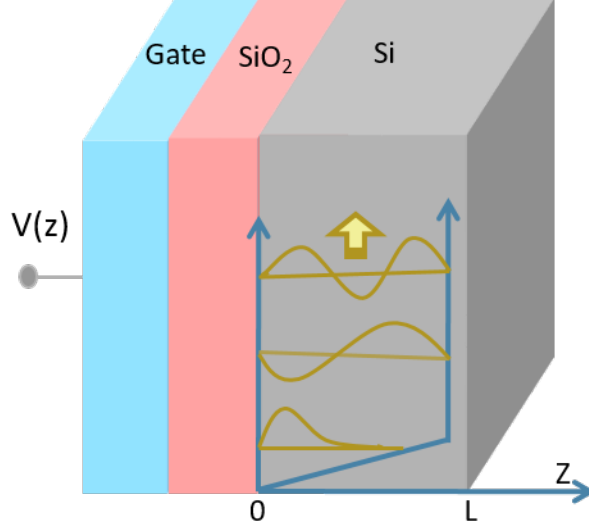
Figure 3.2: Schematic depiction of the simulated silicon nanoribbon. The thickness of the silicon layer is L=20 nm, while the oxide thickness is 10 nm. Gate voltage is applied to the metal gate, causing an inversion layer to appear near the semiconductor-oxide interface. Confinement of carriers and in the near-triangular potential well near the Si surface, and the separation of the confined subbands, are also shown schematically in the figure.

electrostatic potential so that $V_{Schr.}(z) = V(z) + V_{Barrier}$ where $V_{Barrier} = 4.35$ eV for $z < 0$ and $V_{Barrier} = 0$ for $z > 0$. The time-independent Schrödinger equation is then solved in the effective-mass approximation by setting up a finite-difference solution over the same discretization as the Poisson system, only restricting the solution to the silicon region plus a few points in the oxide. The resulting eigenvalue problem [5]

$$H\Psi(z) = V_{Schr.}(z)\Psi(z) \tag{3.2}$$

is solved numerically to obtain eigenvalue/eigenvector pairs at each discretization point. Then the obtained energy values are used to calculate the charges in the obtained bands

$$N = \int D(E)f(E)dE \tag{3.3}$$

Then the charge density is calculated and again used to solve the Poisson equation. The potential profile is then used to solve numerically for the eigenvalue/eigenvector pairs. This self-consistent loop is iterated to till the convergence in the charge density is achieved. Then, the resultant subband energies E_n^b are used to calculate the contribution of each subband to the thermoelectric Seebeck Coefficient (S) using the following relations from the semi-classical Boltzmann Transport Equation (BTE), solved under the Relaxation Time Approximation (RTA) [43] :

$$L^{(\alpha)} = -e^2 \sum_{n,b} \int_0^\infty \frac{\partial f_0\left(E + E_n^b\right)}{\partial E} \left(E + E_n^b - E_F\right)^\alpha \Xi(E) dE \tag{3.4}$$

$$\Xi(E) = \tau_n^b\left(E\right) g_n^b\left(E\right) v_b^2(E) \tag{3.5}$$

where $L^{(\alpha)}$ is called the transport integral, $\Xi(E)$ is called transport distribution function (TDF), E_F is Fermi energy, E_n^b is the subband bottom for band b with subband n, g_n^b is the density of states of that subband, $\tau_n^b\left(E\right)$ is energy dependent relaxation time, and $v_b(E)$ is velocity of the carriers in the ladder b. The Fermi window factor $-\partial f_0\left(E + E_n^b\right)/\partial E$ has to be symmetric [44] with E_F and the $\Xi(E)$ must be as big as possible in the Fermi window to have good thermoelectric properties.

In the effective mass approximation, velocity of carriers ($v_b(E)$) can be written in the form of their corresponding effective mass and energy of the subband as follow

$$v_b(E) = \sqrt{\frac{2E}{m_v^b}} \tag{3.6}$$

where m_v^b is conductivity or transport effective mass for band b. Carrier transport is controlled by the scattering mechanisms that they undergo i.e., from lattice vibrations, impurities, material defects and other electrons. The scattering mechanisms that are implemented in this work are inelastic intervalley scattering by optical phonons ($\tau_{n,O}^b(E)$), elastic acoustic phonon scattering ($\tau_{n,A}^b(E)$) and surface roughness

16

scattering($\tau_{n,S}^b(E)$) [53, 26, 14, 5, 40, 15]. The relaxation time of the carriers $\tau_n^b(E)$ for band b with subband n is obtained by calculating the scattering rates of different scattering mechanisms and combining them by using the Mathiessens rule.

$$\frac{1}{\tau_n^b(E)} = \frac{1}{\tau_{n,O}^b(E)} + \frac{1}{\tau_{n,A}^b(E)} + \frac{1}{\tau_{n,S}^b(E)}. \tag{3.7}$$

In optical phonon intervalley scattering both f-type and g-type processes are implemented. A root-mean-square surface roughness of 0.35 nm is used in the calculation of surface roughness scattering. An acoustic-phonon deformation potential of 12 eV is used for implementing the acoustic phonon scattering. This model has been thoroughly validated against the experimental results in [43]. For intervalley scattering, an optical deformation potentials of 8×10^{10} eV m^{-1} and 11×10^{10} eV m^{-1} with optical phonon energies of 0.059 eV and 0.063 eV are used for f-processes and g-processes respectively.

3.3 Results and Discussion

To check the proposed approach in silicon nanoribbons towards the possible enhancement in Seebeck coefficient (S), we implement the elastic mechanisms, phonon acoustic and surface roughness scattering has to be minimized; thus making the inelastic intervalley optical phonon scattering as dominant mechanism. A reduced acoustic phonon scattering is implemented by using a deformation potential which is 10% of the normal value. All the transport integrals and the Seebeck coefficient S are calculated and shown in Fig. 3.3. As expected, there is a little or no change in S in the presence of surface roughness in normal or reduced acoustic phonon scattering conditions, indicating that the elastic surface roughness (SR) is the dominant scattering mechanism when large roughness is present. At low temperatures (especially at $T < 200K$) there is a significant enhancement in S, particularly in the ideal case

17

when there is no surface roughness. The enhancement is more prominent with reduced acoustic phonon scattering (red color in Fig. 3.3). The restriction to low temperatures is due to the need for optical phonon intervalley scattering to be the dominant mechanism, which occurs at low temperatures. Our proposed approach does lead to enhancement in S, which is attributed to a narrow rectangular window-shaped TDF.
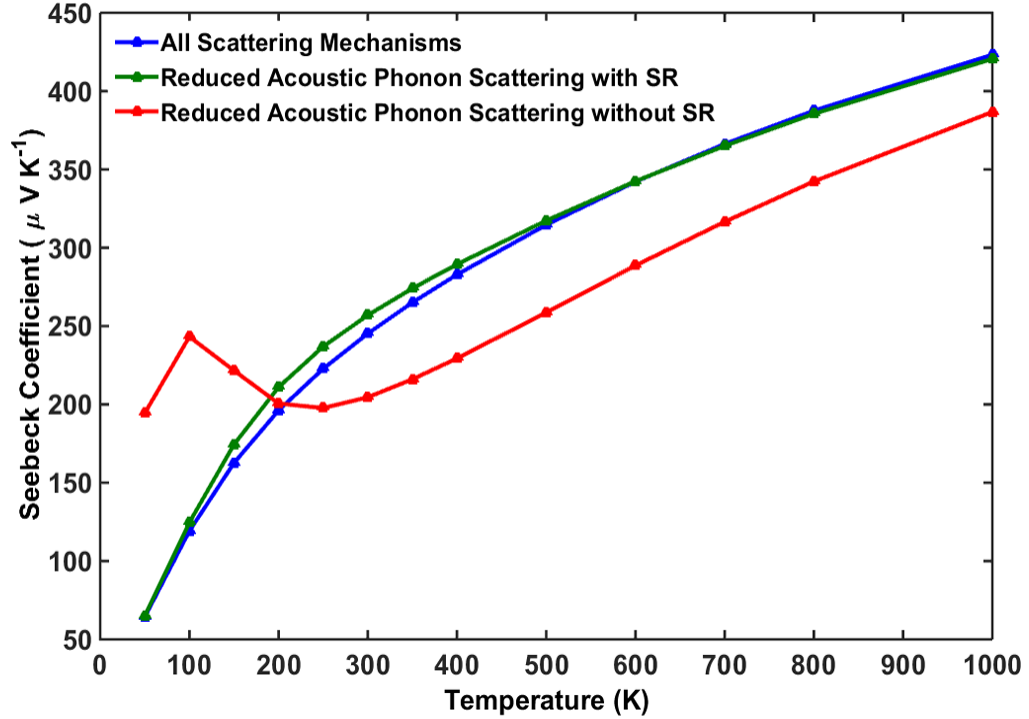
Figure 3.3: S at different temperatures with a V_{gate}= 5V for all scattering mechanisms, reduced acoustic phonon scattering with surface roughness (SR) and without surface roughness. There is an enhancement in S at low temperatures with reduced acoustic phonon scattering without surface roughness.

To validate it, TDF is plotted for the temperature T=100 K where a significant enhancement is observed. Fig. 3.4 plots the TDF which displays a sharp and narrow rectangular peak at low energies and gradually decreases towards the higher energies. Here, inelastic optical phonon scattering is the dominant mechanism, so carriers can only undergo scattering by either emitting or absorbing an optical phonon. Energy

conservation requires that this emitted or absorbed phonon has an energy of $E_{op} = \hbar\omega_{op}$. Typically, emission dominates over absorption in the intervalley optical phonon scattering [41]; the emission rate Γ_{ems} due to inelastic optical phonons is proportional to $\Theta(E+\Delta(E)-E_{op})$; here $\Delta(E)$ is the energy difference of initial and final subbands between which scattering occurs. Electrons occupying lower energies near the bottom of each subband lack sufficient energy to emit an optical phonon, required for this transition, which leads to $\Gamma_{ems}(E < E_{op}) = 0$. This requirement, which stems from energy conservation, delays the onset of the step in the inelastic scattering rate, which leads to the narrow rectangular window shape to the TDF.
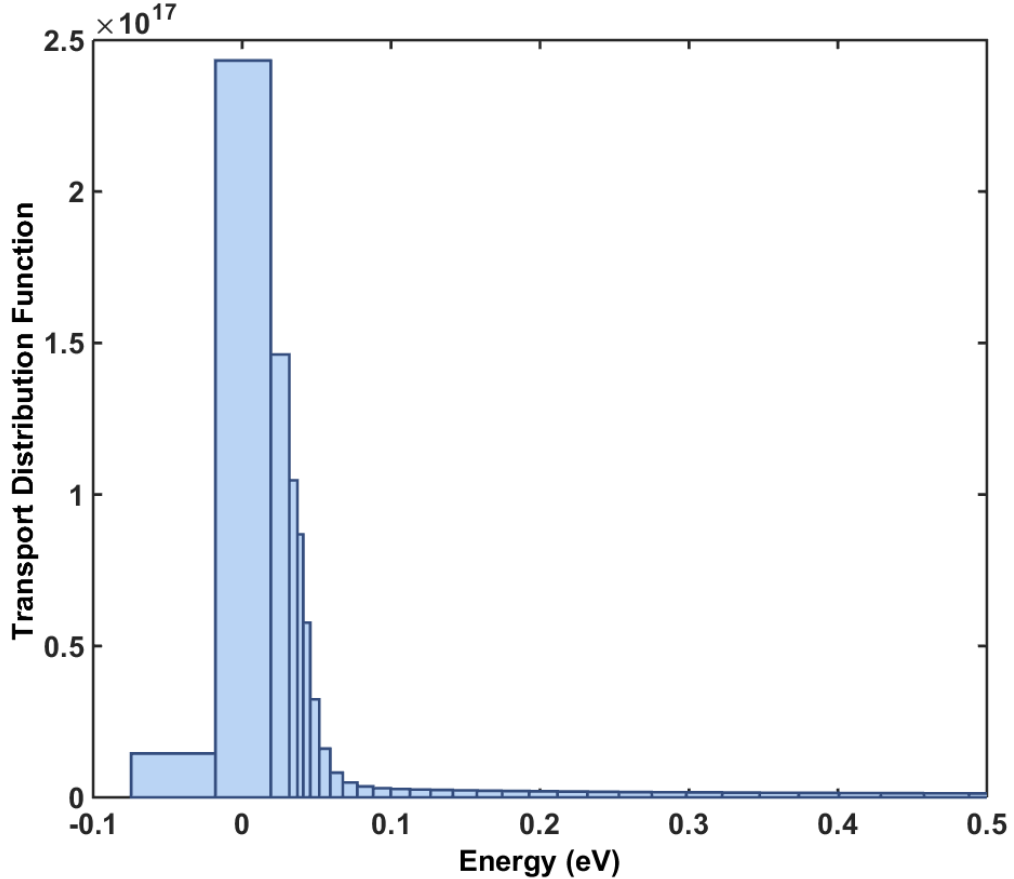
Figure 3.4: Delta shaped Transport Distribution Function (TDF) formed at the second subband with T=100K, V_{gate}=5V and optical phonon energies more than the maximum subband energy gap.

To explore the contribution of narrow rectangular window-shaped TDF towards the enhancement of TE properties, the Seebeck coefficient(S) is calculated at different optical phonon energies (E_{op}) as shown in Fig. 3.5. Here it is shown that the matching between the 5 k_BT "Fermi window" and the optical phonon energy plays a major role in attaining the maximum enhancement in S. Having an optical phonon with energy (E_{op}) comparable to the Fermi window width ($\sim 5k_BT$) utilizes the entire Fermi window; in that case, the narrow TDF matches the Fermi window and produces the largest enhancement of the Seebeck coefficient (S). Our findings here agree with the work of Zhou et. al. [51] and Kim et.al. [24] where the concept of optimal bandwidth was introduced as a way to achieve the maximum energy conversion efficiency. However, with further increase in the optical phonon energy (E_{op}), the optical phonon energy begins to exceed the separation between adjacent subbands and the TDF starts to smear out due to the onset of elastic transitions between subbands. Further improvements were not possible even though the complete Fermi window is utilized, thereby decreasing the enhancement in S which is shown in Fig. 3.5.

Results in Fig. 3.5 were obtained by applying a constant gate voltage V_{gate} of 5 Volts, which fixes the subband separation in the inversion layer. The dependence of subband energies on applied gate voltage also plays an important role in the shape of the TDF and affect the conditions which can lead to Seebeck enhancement. In Fig. 3.6, we have simulated the SiNR at a constant temperature of T=80 K and varied the applied bias. Increasing the gate bias voltage increases the steepness of the potential well inside the semiconductor and produces larger subband separation. The number of carriers in the confined inversion layer is also controlled by the gate voltage, and thereby affects the position of the Fermi level relative to the positions of the subbands. But these changes to the electronic band structure only affects the amount enhancement that can be achieved. The phonon energy where the peak in S falls doesn't change, as it is controlled by the Fermi window which is constant for
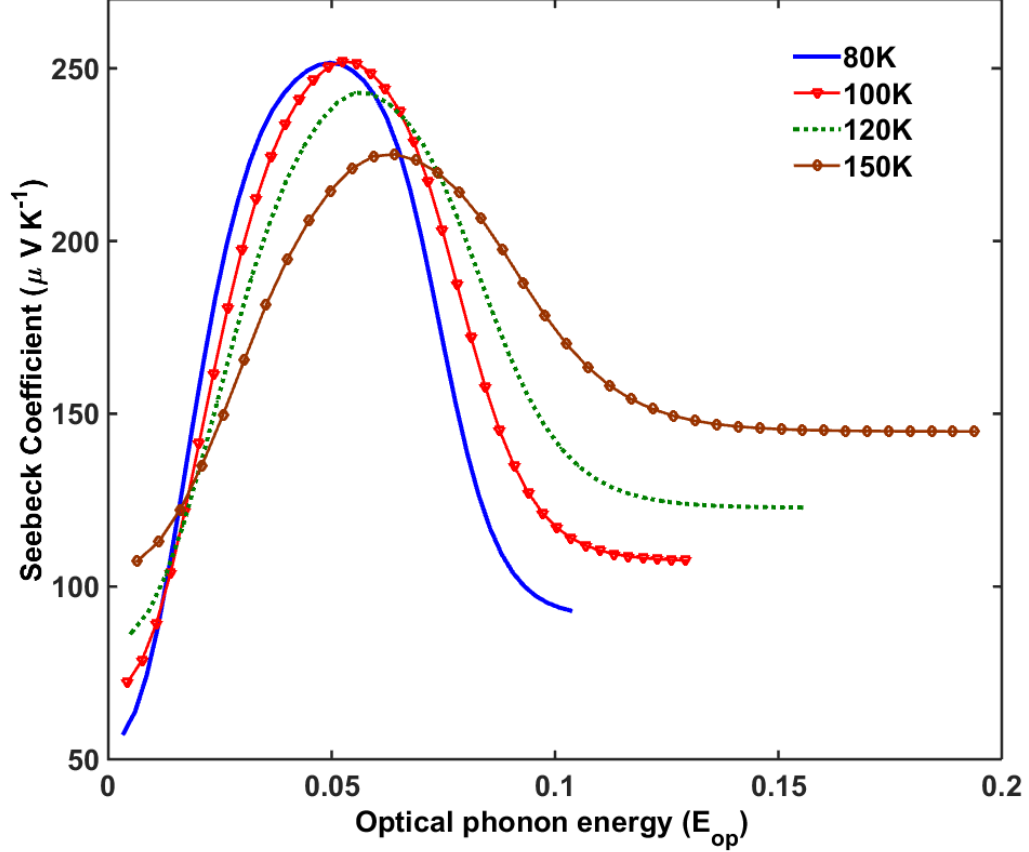
Figure 3.5: Variation in S with optical phonon energies showing the peak being positioned near the valley bottom subband energy difference with $V_{gate}= 5$ V at different temperatures. The change in subband energy difference by temperature is reflected in the shift of peak in S.

a given temperature. We conclude that, at a fixed operating temperature, applying low gate bias and having optical phonon energies which utilize the entire of Fermi window can provide maximum Seebeck coefficient (S).

The height of the steps in the step-like electronic DOS of 2-dimensional confined structures, used here to achieve the narrow window-shaped TDF, depends also on the density of states effective mass (m_d^*). As DOS $\propto m_d^*$, by selecting the material with higher m_d^* we can increase the height of each step in the DOS. However, the increase in m_d^* also implies a corresponding decrease in the subband energy difference, which
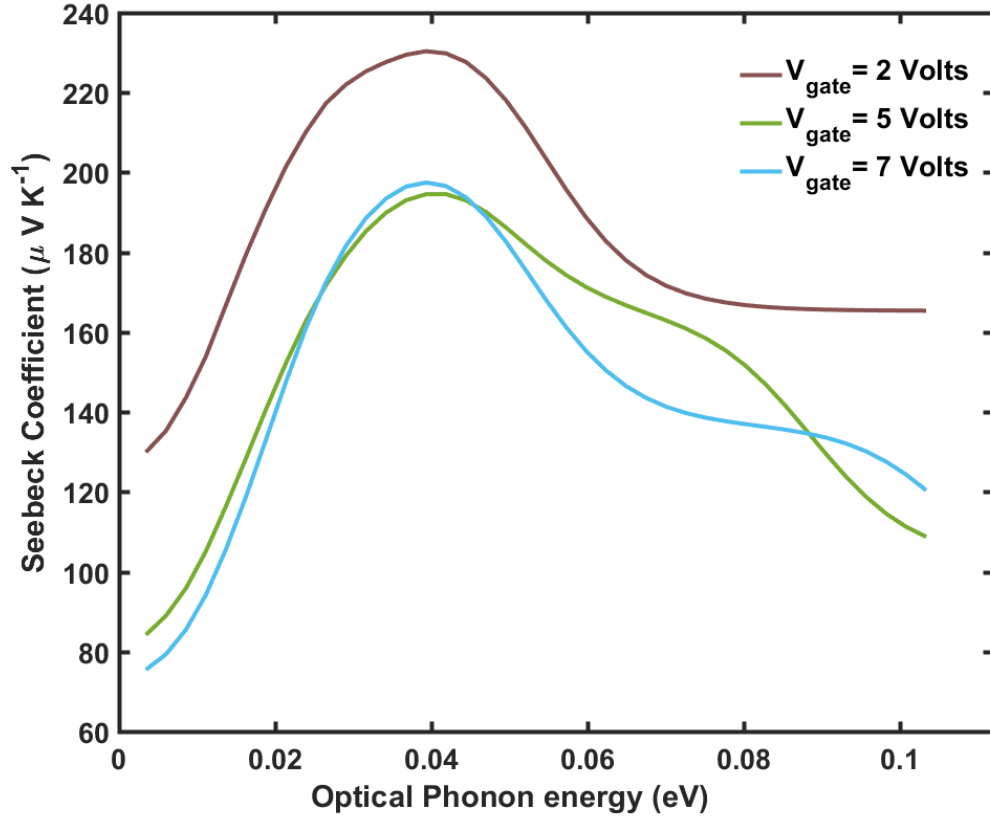
Figure 3.6: Seebeck coefficient as a function of the energy of the optical phonon for several values of gate voltage. The gate voltage controls the number of carriers in the confined inversion layer and thereby affects the position of the Fermi level relative to the positions of the subbands. Higher gate voltage means the charge concentration of electrons is higher and the Fermi level is closer to the lowest subband, which decreases the Seebeck coefficient, as shown in previous work [43].

has been observed to be detrimental to the Seebeck coefficient. To observe this effect, S has been calculated in SiNR with different dominant scattering mechanisms by changing the effective mass and plotted in Fig. 3.7. At low values of m_d^*, there is considerable enhancement which dies off as one moves to higher effective mass. So a careful selection of the material is required to achieve the maximum Seebeck enhancement by balancing the DOS and scattering of carriers. We conclude that higher effective mass materials may be advantageous, as long as they can maintain large subband separations exceeding the optical phonon energy.
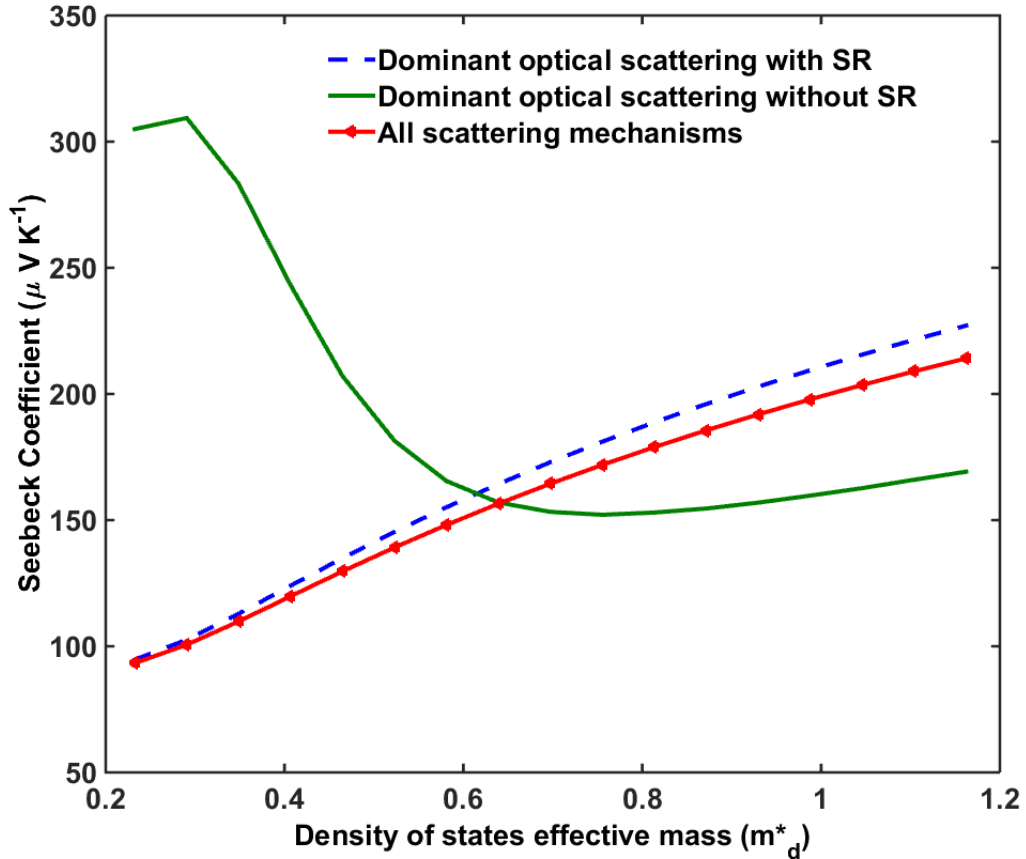
Figure 3.7: Variation in S with the DOS effective mass m_d^* at T=100 K with $E_{optical}$=0.043 eV and V_{gate}=5 V.

3.4 Conclusion

In summary, the selection of the material for maximum energy conversion at a given temperature depends on the interplay between the subband structure and effectively using the inelastic scattering mechanisms to take the advantage of such subband structure. Simulation for thermoelectric conversion coefficients in a silicon nanoribbon showed an enhancement in Seebeck coefficient at low temperatures in situations where inelastic transitions are dominant and little or no elastic interactions in the form of acoustic and surface roughness scattering. A further detailed study showed the formation of almost delta shaped transport distribution function due to the discrete band structure in confined nanostructures that restricts the elec-

tron transport to the lowest subbands. This forces electrons to acquire or emit the required energy to occupy these energy levels after scattering which is assisted by the optical phonons due to the dominant intervalley optical phonon scattering. In addition to that, we observed that a delta shaped TDF alone can't provide maximum enhancement, the Fermi window decides the extent of this enhancement. Furthermore, by applying external gate bias and thereby rearranging the subbands, we can achieve further control on enhancement in the thermoelectric Seebeck coefficient by tuning the TDF. Changing the density-of-states effective mass affects the height of the step in the TDF and further tunes the enhancement; however, the corresponding change in the subband structure limits the advantage from reduced effective mass.

In our study, the 2D nature is imparted by confining a bulk material and the applied gate voltage controls the spacing in the discrete band structure, thereby creating a strong interdependence that affects the enhancement. So, to avoid it an intrinsically 2D material can be used which will have an independent native discrete band structure and then a detailed analysis in such material gives more insight on proposed method for achieving thermoelectric enhancement. A possible extension to this work can be implementing our approach in such 2D materials to observe the nature of the enhancement and formulating a general criteria to design an efficient thermoelectric device.

CHAPTER 4

ENHANCEMENT OF SEEBECK COEFFICIENT IN RAPID VARYING PERIODIC STRUCTURES USING WIGNER FORMALISM

4.1   Introduction

Electron filtering is one of the approaches that can provide an improved thermo-electric performance. In electron filtering "cold" electrons (low energy electrons) are restricted from participating in transport using a potential barrier as the Seebeck co-efficient $(S) \propto (E - E_f)$. There have been several studies done by implementing this approach using nanocomposites [25], superlattices, single and multiple barrier structures. Zide et al. [52] demonstrated an increase in thermoelectric efficiency using a nanocomposite consisting of III-V semiconductors (more specifically, InGaAlAs) containing nanoparticles of erbium arsenide as energy-dependent scatterers. Yokomizo and Nakamura [49] showed ZGNR/h-BN superlattices drastically enhance the Seebeck coefficients of ZGNR's. Dragoman and Dragoman [12] showed that the Seebeck coefficient in a graphene-based interference device can be engineered to achieve unprecedented high values. Fig. 4.1 shows the Graphene device has been used by them with a series of gates which are used to create a periodic potential in Graphene. Then they studied the effect of such periodic potentials on the thermoelectric performance of the device and showed a giant Seebeck coefficient being achieved. There are studies ([36], [35] and [25]) based on NEGF formalism to study the effect of smoothness and periodicity of potential barriers on thermoelectric parameters. In addition to these direct implementations, potential barriers are used to model the grain boundaries in nanocrystalline materials [37]. In this thesis, we implemented such periodic potential

25

in semiconducting materials and study their effects on thermoelectric performance. We used a comprehensive transport model that can effectively capture the carrier-potential interactions using Wigner formalism along with the semiclassical Boltzmann transport equation (BTE).
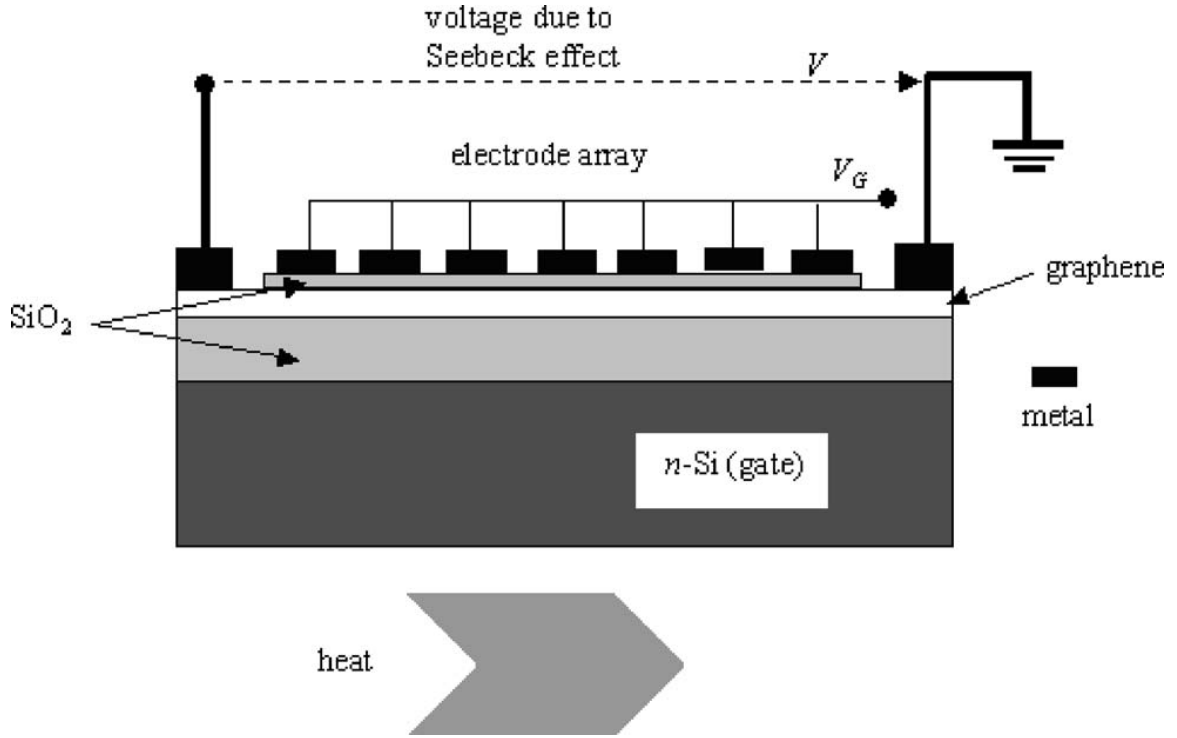
Figure 4.1: The graphene device used by D. Dragoman and M. Dragoman [12] to observe the effect of periodic potential being applied using a series of gates.

4.2 Wigner Formalism

The semi-classical approach of the Boltzmann transport equation (BTE) is widely used in the device simulations. But, in semi-classical approach, electrons are considered as point particles moving with a velocity of their wave packet center and the spread of wave packet to be unchanged during their propagation. Hence the electrons are assumed to be well localized wave packets of Gaussian typical form. Along with that the potential across the simulation domain is linear, quadratic or varies slowly. But, this semi-classical approach is unable to explain all the device effects

26

(such as underestimating the threshold voltage in Bulk MOSFET in ultra-thin body transistors [10, 47]) and quantum processes like interaction of carriers with the rapid potential changes across the materials such as super lattices. To model such abrupt change in the potential across the material, quantum formalisms like density matrix, Wigner function and Green's function approaches have to be used. In this thesis, to capture the quantum effects, Wigner function is used which effectively captures the potential variation and its effect on distribution of carriers across the material. The Wigner equation is given as [34, 46]

$$\left(\frac{\partial}{\partial t} + v_r \nabla_r + \frac{eF}{\hbar} \nabla_k\right) f_w(r, k, t) = Q f_w(r, k, t) + \left(\frac{\partial f_w}{\partial t}\right)_{coll} \tag{4.1}$$

where $f_w(r, k, t)$ is called as Wigner distribution function which is written as

$$f_w(r, k, t) = \frac{1}{2\pi} \int dr' e^{-ir'k} \rho\left(r + \frac{r'}{2}, r - \frac{r'}{2}\right) \tag{4.2}$$

where ρ is the density operator that is used to represent the mixed states in the quantum system, r and r' represents the center of mass and spread of the wave packet. The potential operator or quantum evolution $Q f_w(r, k, t)$ is given as

$$Q f_w(r, k, t) = \int dk' V_w(r, k - k') f_w(r', k, t) \tag{4.3}$$

Where the Wigner potential is given as

$$V_w(r, k) = \frac{1}{i\hbar(2\pi)^d} \int dr' e^{-ir'k} \left(V\left(r + \frac{r'}{2}\right) - V\left(r - \frac{r'}{2}\right)\right) \tag{4.4}$$

which depends on the potential V across the material. Eq. 4.4 can be simplified as

$$V_w(r, k) = \frac{2}{\pi\hbar} Im\{e^{2ikr} \hat{V}(2k)\} \tag{4.5}$$

27

where $\hat{V}(k)$ is spatial Fourier transform of V_q

$$\hat{V}(k) = \int\limits_{-\infty}^{\infty} V_q(r)e^{-ikr}dr \tag{4.6}$$

The potential operator $Qf_w(r, k, t)$ can be decomposed in to slow varying classical component and rapidly varying quantum mechanical component based on V.

$$V(x) = V_{cl}(x) + V_{qm}(x) \tag{4.7}$$

The contribution towards V_{cl} from the slow varying potential like applied external bias that is taken care in BTE. Also, barriers cause the rapid varying V_{qm} which is handled by the Wigner function. Hence the Wigner equation tends to the Boltzmann equation in the case for which the Boltzmann equation is established i.e. linear, quadratic or slowly varying potential. The Boltzmann equation may thus be seen as the semi-classical limit of the Wigner equation and at steady state with a small perturbation (g_w where $f_w = f_o + g_w$) to distribution, can be implemented by using the Wigner-Boltzmann transport equation (WBTE) which is given as

$$\left(v_r\nabla_r + \frac{eF}{\hbar}\nabla_k\right)f_w(r, k, t) = Qf_w(r, k, t) + \left(\frac{\partial f_w}{\partial t}\right)_{coll} \tag{4.8}$$

4.3 Soution to Wigner-Boltzmann transport equation (WBTE)

4.3.1 Rode's Method for Boltzmann Transport Equation (BTE)

To model the electron transport by solving the Boltzmann Transport Equation (BTE), Rode's method can be used. Rode's method [42] is an iterative method to calculate electronic characteristics of a material by solving for perturbation to the distribution function due to the applied field. Then this perturbation is used to calculate electrical transport parameters like the Seebeck coefficient (S), electrical conductivity

(σ), electron thermal conductivity(κ_{el}) etc. The collision operator in BTE (Eq. 2.1) includes the evolution of the particles from scattering mechanisms. This evolution caused by the perturbation in the distribution of carriers can be obtained easily in the absence of any inelastic processes using RTA approximation (Eq. 2.2) for collision operator in BTE. In the presence of dominant inelastic scattering process, the concept of RTA is not accurate as the distribution of carriers doesn't relax to their equilibrium distribution. So Rode's method has to be used, which effectively models inelastic processes in the material.

In Rode's method, all inelastic scattering processes of carriers is included while solving for the perturbation to the distribution function. To do that the distribution function is approximated to first order using Lagrange polynomials

$$f(k) = f_o(k) + \sum_{n=1} g_n(k)p_n\left(cos(\theta)\right) \tag{4.9}$$

where $f_o(k)$ is equilibrium distribution function, $g_n(k)$ is the perturbation to the distribution function due to the applied electric field and θ being the angle between carrier velocity and electric field. The collision term in Eq. 2.1 can be written as sum of contribution from elastic and inelastic scattering processes.

$$\left(\frac{\partial f}{\partial t}\right)_{coll} = \left(\frac{\partial f}{\partial t}\right)^{el}_{coll} + \left(\frac{\partial f}{\partial t}\right)^{inel}_{coll} \tag{4.10}$$

Including both in-scattering and out scattering processes of inelastic scattering mechanisms, its contribution can be written as

$$\left(\frac{\partial f}{\partial t}\right)^{inel}_{coll} = cos(\theta)\left[I(k) - g(k)I_o(k)\right] \tag{4.11}$$

$$I(k) = \sum_{k'} g(k')cos(\alpha)\left[S^{inel}_{kk'}f_0 + S^{inel}_{k'k}(1 - f_0)\right] \qquad \text{inscattering processes} \tag{4.12}$$

29

$$I_o(k) = \sum_k \left[S_{k'k}^{inel} f_0' + S_{kk'}^{inel} (1 - f_0') \right] \qquad \text{outscattering processes} \qquad (4.13)$$

and the contribution from elastic mechanisms can be written as

$$\left(\frac{\partial f}{\partial t} \right)_{coll}^{el} = \frac{g(k) cos(\theta)}{\tau^{el}(k)} \qquad \text{outscattering processes} \qquad (4.14)$$

where α is the angle between the initial and final wavevector, $S_{k'k}$ is the scattering rate from k' to k, f_0 is the Fermi-Dirac distribution of corresponding wavevector and $\tau^{el}(k)$ is the elastic processes relaxation time. Substituting Eq. 4.10 in Eq. 2.1, perturbation in distribution can be written as

$$g(k) = \frac{I(k) + \frac{eF}{\hbar} \frac{\partial f_0}{\partial k} - v_r \frac{\partial f}{\partial r}}{S_0(k)} \qquad (4.15)$$

$$\text{where} \qquad S_0(k) = I_0(k) + \frac{1}{\tau^{el}(k)} \qquad (4.16)$$

S_0 is the sum of out-scattering rates of all processes and in-scattering rates of all scattering mechanisms except inelastic mechanisms. The perturbed distribution function for electrons is calculated by iteratively solving,

$$g_{i+1}(k) = \frac{I(k) + \frac{eF}{\hbar} \frac{\partial f_0}{\partial k} - v_r \frac{\partial f}{\partial r}}{S_0(k)} \qquad (4.17)$$

$$\text{where} \qquad I(k) = \sum_{k'} g_i(k') cos(\alpha) \left[S_{kk'}^{inel} f_0 + S_{k'k}^{inel} (1 - f_0) \right] \qquad (4.18)$$

Here the ith iteration solution of g_i is used to calculate the $(i+1)^{th}$ solution of the perturbed distribution function and the process is continued till it converges. The zeroth-iteration solution g_0 is assumed to be 0, where the solution gives the RTA

approximated value. Then the mobility and Seebeck coefficient are calculated using converged g_i as follows:

$$\mu_e = \frac{\int \int v(k) g_i(k) \delta(E - E(k)) dk\, dE}{eF \int \int f(k) \delta(E - E(k)) dk\, dE} \tag{4.19}$$

$$S = \frac{\int \int v(k) g_i(k)(E - E_f) \delta(E - E(k)) dk\, dE}{T \int \int v(k) g_i(k) \delta(E - E(k)) dk\, dE} \tag{4.20}$$

where $v(k)$ is group velocity of carriers, F is applied electric field, E_f is Fermi energy level and T is the temperature of the material.

4.3.2 Rode's implementation of the WBTE

The Wigner-Boltzmann transport equation (WBTE) is implemented here using the Rode's method to calculate the perturbation to the distribution function due to the rapid varying potentials. In the Rode's implementation of the WBTE, the contribution of rapid varying potentials is evaluated as an additional force term being added to the conventional force due to the electric field. The perturbation to the distribution function in Eq. 4.17 can be written as

$$g_{i+1} = \frac{S_{io} g_i + \frac{eF}{\hbar} \frac{\partial f_0}{\partial k} - v_r \frac{\partial f}{\partial r} + Q f_w}{S_0} \tag{4.21}$$

where $Q f_w$ is the potential operator or quantum evolution of Wigner potential.

In this thesis, an extensive study of effect of rapid varying periodic potentials of different periodicity and shape is done as shown in Fig. 4.2. The reason for a rapid varying periodic potential is to limit position dependence and complexity of solution of the potential operator or quantum evolution term at a fixed position for a single electron packet. Let's consider a generalized periodic fast-varying potential of form,

$$V_q(r) = \sum_{n=-\infty}^{\infty} V_p(r - nL_p) \tag{4.22}$$

31

The quantum evolution (Eq. 4.3) (detailed derivation is shown in Appendix B) of this generalized periodic potential is

$$Qf_w = \sum_{m=1}^{\infty} W_m(r) \left[f_w\left(r, k - \frac{m\pi}{L_p}\right) - f_w\left(r, k + \frac{m\pi}{L_p}\right) \right] \tag{4.23}$$

where for a square barriers of height V_0 with smoothening factor β and width $2a$ or $L_p/2$ (Fig. 4.2)

$$V_q(r) = \frac{V_0}{2} \left\{ -erf[\beta(r - a)] + erf[\beta(r + a)] \right\} \tag{4.24}$$

$W_m(r)$ is obtained as

$$W_m(r) = \frac{2V_0}{\pi \hbar m} e^{\frac{-m^2 \pi^2}{\beta^2 L_p^2}} sin\left(\frac{2\pi m a}{L_p}\right) sin\left(\frac{2\pi m r}{L_p}\right) \tag{4.25}$$
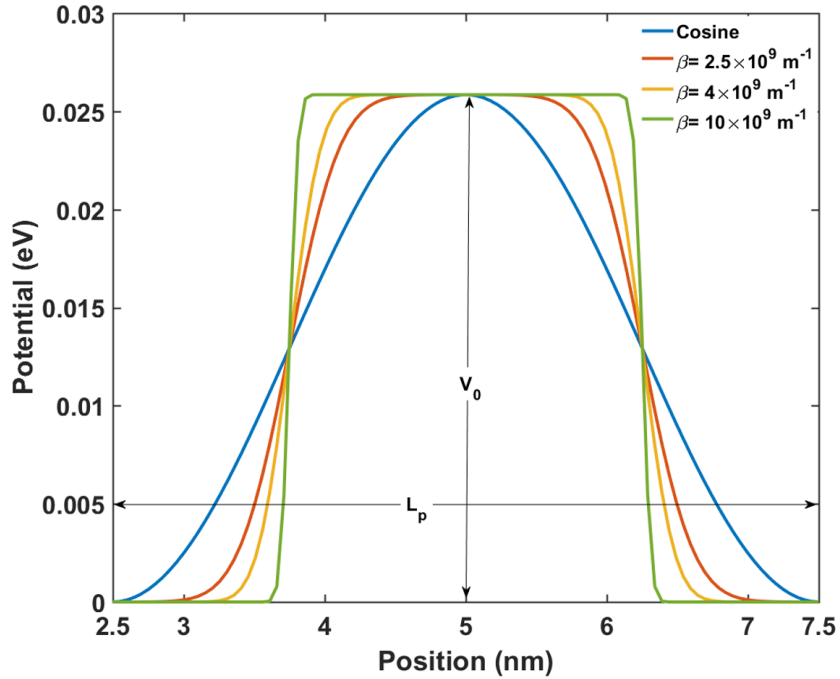

Figure 4.2: Shape of the potentials that are being considered in this study and their shape parameters.

In perfectly smooth potentials, a cosine shaped potential $V_q(r) = A \, cos(K_0 r)$, (applied in r direction) where $K_0 = 2\pi/L_p$ has a simple quantum evolution as it has single order Wigner potential which is calculated using the Eq.4.4 (detailed derivation is shown in Appendix B) as

$$V_w = \frac{A \, sin(2K_0 r)}{\pi \hbar} \left[\delta(2k - K_0) + \delta(2k + K_0) \right] \tag{4.26}$$

and the quantum evolution in Eq. 4.3 for cosine potential is obtained as

$$Q f_w = W_m(r) \left[f_w \left(r, k - \frac{K_0}{2} \right) - f_w \left(r, k + \frac{K_0}{2} \right) \right] \tag{4.27}$$

$$\text{where} \qquad W_m(r) = \frac{A \, sin(K_0 r)}{\pi \hbar} \tag{4.28}$$

The Wigner distribution function used in above formulations to calculate the quantum evolution term can be written as

$$f_w(r, k, t) = f_0(r, k, t) + g_w(r, k, t) \tag{4.29}$$

which is the sum of equilibrium distribution function from Fermi-Dirac statistics, and perturbation to distribution due to the electric field and rapid potential variation (as shown in Eq. 4.7). This shows the nonlinearity of WBTE, hence using the Rode's iterative method the perturbation distribution is evaluated at i^{th} iteration and then the quantum evolution for $(i + 1)^{th}$ is calculated as shown in Eq. 4.21 with solution of ith iteration. This process can be repeated till convergence is achieved.

4.4   Implementation of Transport Model

In this thesis, Rode's approach of Wigner-Boltzmann transport formalism is implemented in bulk silicon. To maintain a more realistic approach to the implementation,

the full band structure silicon is used for modeling the thermoelectric properties. To calculate the band structure, the empirical pseudopotential model is implemented and energy $E(k)$ values are calculated for k-space corresponding to $1/8^{th}$ of the Brillouin zone, which can be extended to full BZ using symmetry. Then the energy gradients are calculated to determine the group velocities of electrons. By using this full band structure data, the accuracy of the calculations increases when compared to using the effective mass approximation for carrier energies. Then the density of states (DOS) is calculated using the Spherical averaging method (SAVE) [13]. Then the scattering rates are calculated from the bandstructure and the density of states. The scattering rates that are covered in this model are:

- Elastic Mechanisms

  - Deformation potential acoustic phonon scattering

  - Ionized Impurity scattering

  - Boundary scattering

- Inelastic Mechanisms

  - Intervalley optical phonon scattering (f-type and g-type processes)

Once scattering rates are calculated, then the drift component of Eq. 4.21 is calculated. The model in this thesis is written for a single period length of the potential (either cosine shaped or general square potential). The length of the material along with the rapid varying potential is discretized for the simulation. Then the quantum weight $W_m(r)$ is calculated at every point in the grid, from where the convergence for g_i is started.

As Rode's method uses in-scattering of the inelastic mechanisms for calculating the perturbation in distribution function, it has to be implemented carefully. For any band the inelastic mechanism used here i.e., intervalley optical phonon scattering

34

can have the in-scattering contributions from other three branches and from the same branch. To include this we again used the spherical averaging method [13] to calculate $I(k)$. For example, for f-type emission the $I(k)$ is calculated using SAVE method with $\Lambda_{inems}(k')g_i(k')$ as an weight using Eq. A.5 and Eq. 4.18, where DOS is written as $\int dk\,\delta(E - E(k))$. So,

$$I(k) = \int dk'\Lambda_{inems}(k')\,g_i(k')\,\delta(E_i + \hbar\omega_0 - E(k'))\tag{4.30}$$

where the $E(k')$ is the band from which the carrier scatters to the band E_i. g_i is the perturbed distribution function of the ith iteration and $\hbar\omega_0$ is the optical phonon energy. The coefficient Λ_{inems} for a f-type intervalley scattering can be written as using Eq. A.5 as

$$\Lambda_{inems} = \frac{e\,(N_0 + 1 - f(k))\,(Z - 2){D_0}^2}{\rho\omega_f}\tag{4.31}$$

where N_0 is phonon Bose-Einstein distribution, $f(k)$ is the Fermi-Dirac statistics for electron., D_0 is the optical coupling potential for f-type processes, Z is the degeneracy of silicon, ρ is density and ω_f is the frequency of f-type phonons. This method is used to calculate the in-scattering contribution from intervalley optical phonon scattering by both f and g processes for a band from other three bands and from itself. S_0 in Eq. 4.17 is calculated as follows:

$$S_0 = S_{acs} + S_{imp} + S_b + S_{iop}^o\tag{4.32}$$

S_{acs} is deformation acoustic phonon scattering rate, S_{imp} is impurity scattering rate, S_b is the boundary scattering rate and S_{iop}^o is out-scattering rate of inelastic intervalley phonon scattering. To evaluate the contribution from rapid varying potential in Eq. 4.27 and 4.23, the k vector displaced $g_i(k^+)$ and $g_i(k^-)$ is calculated by interpolating $g_i(k)$. As our simulation domain is fixed to $1/8^{th}$ of the Brillouin zone (BZ), any

query for out of the domain perturbation function is fulfilled by folding the k vector back in to simulation domain using the periodicity of BZ. In this process, the folded k^+ or k^+ vector's final velocity is compared with the k and if they are opposite then the direction of the perturbation is also negated. At each and every iteration towards the convergence, previous iteration value of g_i is used to calculate the $I(k)$ and the quantum evolution term.

The iterative Rode's method to solve for g_i is a nonlinear problem, due to the diffusion term of Eq. 4.21. So, Gummel's iteration method is used to decouple the problem. At first, we solve for g_i without the diffusion term as shown in Eq. 4.33 and a converged solution is obtained.

$$g_{i+1} = \frac{S_{io}g_i + \frac{eF}{\hbar}\frac{\partial f_0}{\partial k} + Qf_w}{S_0} \tag{4.33}$$

Then this solution is used to calculate the diffusion contribution or diffusion term of the transport. The spatial gradient of distribution in the diffusion term is performed using three-point scheme along with the central finite differences. Then we solve for g_i of Eq. 4.21 iteratively, which is now a linear problem. In addition to this for potentials with higher amplitude, the potential is applied in steps to calculate the quantum evolution. Starting at low potentials quantum weight is calculated, from there the partially converged g_i as in Eq. 4.33. Then the amplitude of the potential is incremented in steps along with its partially converged g_i is calculated, till the amplitude reaches the required value. The calculated perturbed distribution function is then used mobility and Seebeck coefficient of electrons is calculated using Eq. 4.19 and Eq. 4.20.
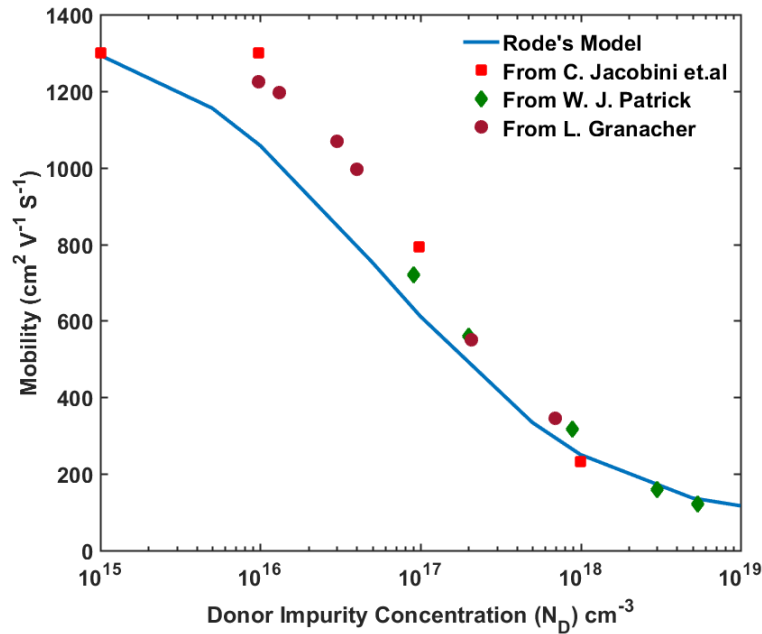
4.5 Results

4.5.1 Validating the Model

Our initial implementation of the Rode's method is completed, and thermoelectric parameters are calculated. At first, to validate the model, bulk silicon thermoelectric properties are compared with the experimental results in the literature. Fig. 4.3a and Fig. 4.3b shows the mobility and Seebeck coefficient dependence on impurity concentration that has been calculated from Rode's implementation, compared with the literature. These thermoelectric parameters are in good agreement with the literature, thus validating the model.

4.5.2 Effect of boundaries on bulk silicon

The aim of this thesis is to study the effects of nanostructuring on thermoelectric properties, now with the model validated the effect of confinement or boundaries is studied. In Nanostructures, material dimensions confine the electron transport and considerably change the electrical characteristics. Our model captures the effect of boundaries on transport through boundary scattering, which evaluates the boundary as either diffuse or specular based on the surface roughness. Then boundary scattering rate is calculated as shown in Appendix A. Fig. 4.4a shows the effect of boundaries when moving from bulk to nanostructures by reducing the width of the simulated silicon sample.

There is a significant decrease in the mobility from bulk to nanostructures due to the increased scattering of electrons at the boundaries as boundary scattering $S_b \propto v/L$. The onset of boundary dependence on electron transport is when the material dimension is less than mean free path (MFP) of the electron, as electrons encounter a boundary before obtaining equilibrium state. To understand this, relative contribution of electrons with different MFPs to electrical conductivity in bulk silicon sample is observed which is shown in Fig. 4.4b, where normalized cumulative electrical

(a) Dependence of mobility of electrons on impurity concentration in bulk silicon at room temperature $T = 300$ K and compared with results from literature C. Jacobini et al., [23] W. J. Patrick [38] and I. Grancher [18].
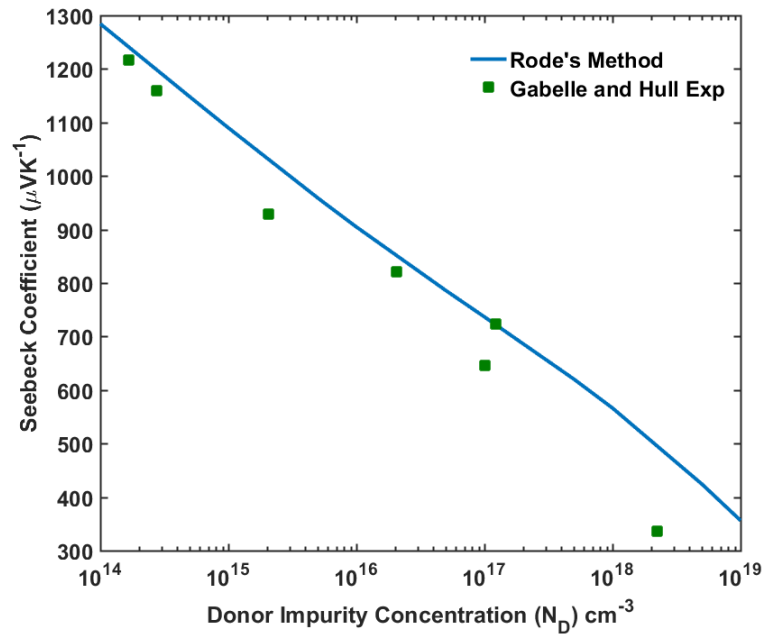
(b) Seebeck coefficient of electrons dependence on impurity concentration in bulk silicon at room temperature $T = 300$ K and compared with results from T. H. Gaballe.et al., [16].

Figure 4.3: Mobility and Seebeck coefficient of silicon are calculated and compared with literature to validate the Rode's method

conductivity from electrons with different MPF is plotted. It shows that the transport is through electrons that have $MFP < 70\,nm$ and $MFP < 30\,nm$ in the silicon for a donor doping concentration of $N_D = 10^{16}\,cm^{-3}$ and $N_D = 10^{19}\,cm^{-3}$ respectively. So, if the silicon sample has a width less than these MFP's, it affects the electrical properties of the material. Another factor that affects the boundary scattering is the surface roughness of the material, as it decides the nature of the boundary as seen by the electrons. When we calculated the change in mobility due to the surface roughness, it didn't show any dependence. In Fig. 4.5a, the mobility of silicon at different surface roughness shows little or no change, this happens when the boundary is diffuse i.e., $p = 0$ in Eq. A.5. Electrons see a boundary as diffuse when the low wavelength or high-momentum electrons heavily contribute to transport. To validate this, electron momentum contribution towards the electrical conductivity is calculated and plotted in 4.5b. It shows that high-momentum electrons that are near Brillouin zone edge ($\approx 2\pi/a = 11.5 \times 10^9\,m^{-1}$) contribute more towards the transport. This can be explained by silicon's conduction band edge minimum being at the Δ valley, and electrons near CB minimum have a major contribution to the transport. So, in silicon, the dimension of boundaries affects transport as we move to nanoscale but the surface roughness has little or no effect on it.

4.5.3 Electron filtering using potential barriers

4.5.3.1 Effect of potential period length (L_p)

To analyze the electron filtering using a potential barrier, Rode's method along with Wigner formalism is used to study the thermoelectric properties as shown in the previous section. Now moving to analyzing the electron filtering and other quantum effects due to the potential barriers, we first observed the effect of period (L_p) of a smooth potential barrier like a cosine function. After solving for the perturbed distribution function (Eq. 4.21) including the quantum evolution due to this cosine
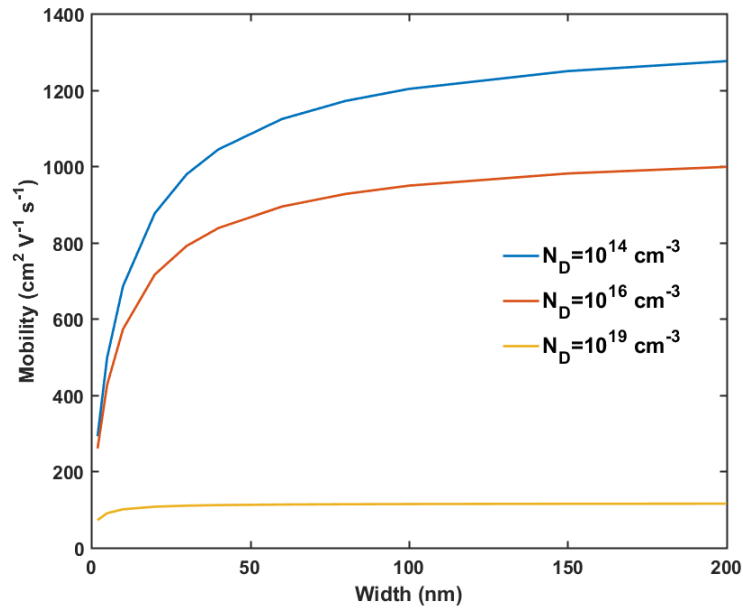
(a) Width dependence of mobility to show the onset of effect of boundaries on electrical characteristics in bulk silicon at room temperature $T = 300$ K for different doping concentrations.
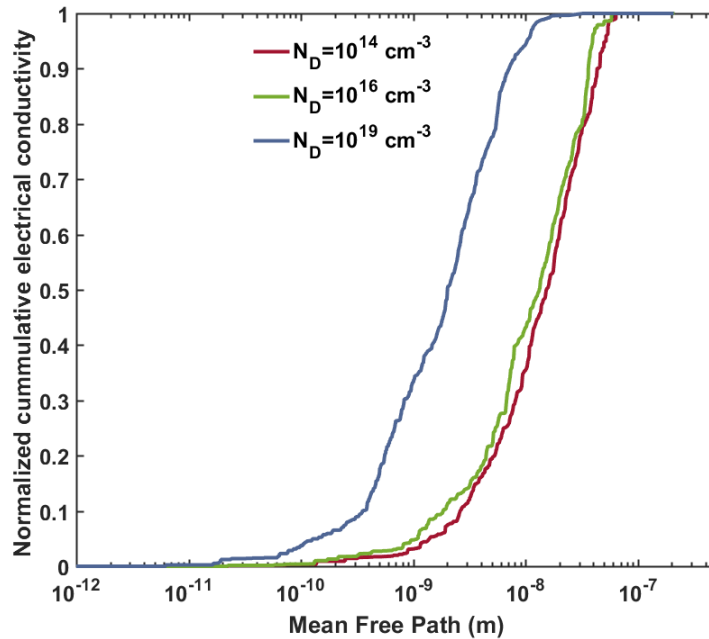
(b) Contribution of electrons with different MFP's to electrical conductivity in bulk silicon sample at a temperature of $T = 300$ K to predict the onset of boundaries effect on electron transport.

Figure 4.4: Change in electrical properties of silicon as move to nanoscale (as we reduce the device dimension) and using MFP of electrons to predict this dependence.
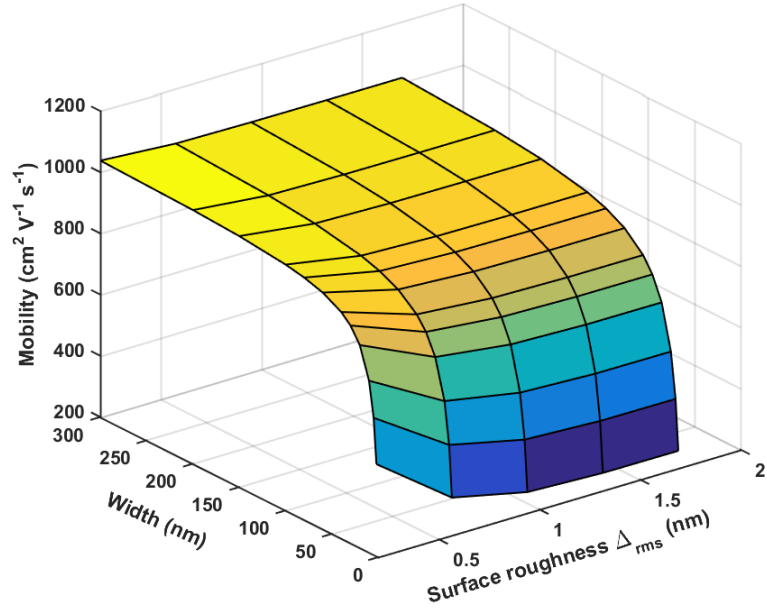
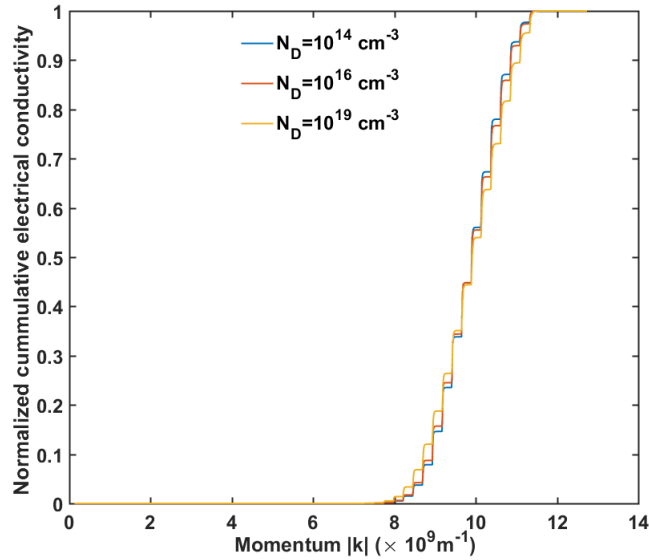(a) Effect of boundaries on mobility of electron at a concentration of $N_d = 10^{16}$ cm^{-3} and at a temperature of $T = 300$ K. Mobility decreases with decrease in width of the sample due to the increase in boundary scattering of electrons, although the surface roughness has minimal effect on the transport.


(b) Momemtum of electrons that contribute to electrical conductivity at a temperature of $T = 300$ K showing that only high momentum electrons contribute to transport, thus creating a diffuse boundary in bulk silicon. This explains the little or no effect of boundary roughness on mobility in 4.5a.

Figure 4.5: Effect of boundary surface roughness on the electron transport in silicon.

potential (Eq. 4.27), thermoelectric parameters are calculated. Here a donor concentration of $N_D = 4 \times 10^{19}\, cm^{-3}$ is used which corresponds to a Fermi level of $0.0072\, eV$ above conduction band edge E_C (E_c is set to zero) with a barrier height of $V_0 = 1\, k_B T$. Fig. 4.6a shows the decrease in the Seebeck coefficient with an increase in the period of the potential barrier. This behavior can be attributed to the reduction in tunneling and energy filtering playing a major role with an increase in period lengths. On the other, hand electrical conductivity also decreases with barrier height as shown in Fig. 4.6b. To understand these effects, energy dependence on electrical conductivity and Seebeck coefficient is calculated which is shown in Fig. 4.7.

Fig. 4.7a and Fig. 4.7b shows the contour plot for energy dependence on conductivity, potential profile (red dotted line) and the quantum weight (white dotted line) to the Wigner contribution with respect to the position in the material. At lower periods of the potential barrier, there is conduction of electrons due to tunneling along with the electron filtering. But, moving from $L_p = 3\, nm$ to $L_p = 9\, nm$ this conduction due to tunneling of electrons at low energies is restricted. This results in a decrease in electrical conductivity with increase in barrier width even though the effect of electron filtering doesn't change due to constant barrier height. This trend in electrical conductivity is consistent even with the change in the barrier height as observed in Fig. 4.7c and Fig. 4.7d.

Coming to the effect on Seebeck coefficient, as explained before at lower barrier width tunneling dominates the electron conduction which results in higher Seebeck coefficient. But as we move to higher widths Seebeck coefficient is only effected by electron filtering due to the barrier (i.e conduction is only over the barrier and no tunneling as shown in Fig. 4.7b). The position dependence of Seebeck coefficient (dotted line) and their energy dependence (shown as contour) at different barrier widths is shown in Fig. 4.7e and Fig. 4.7f, which shows maximum contribution near the peak of the potential barrier. But, there is a small shift in that peak and the
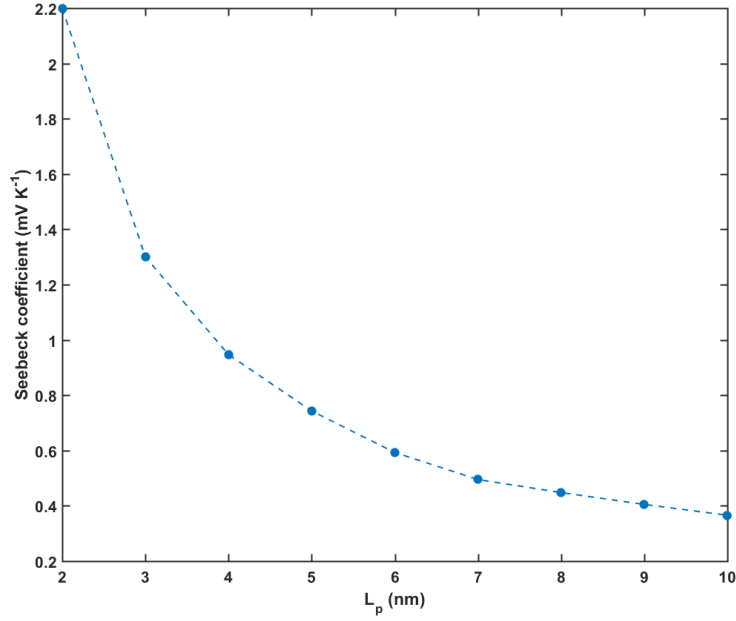
(a) Seebeck variation due to the change in the period length (L_p) of the potential barrier showing the transition from tunneling dominant transport at lower periods to just energy filtering due to the barrier at higher periods.
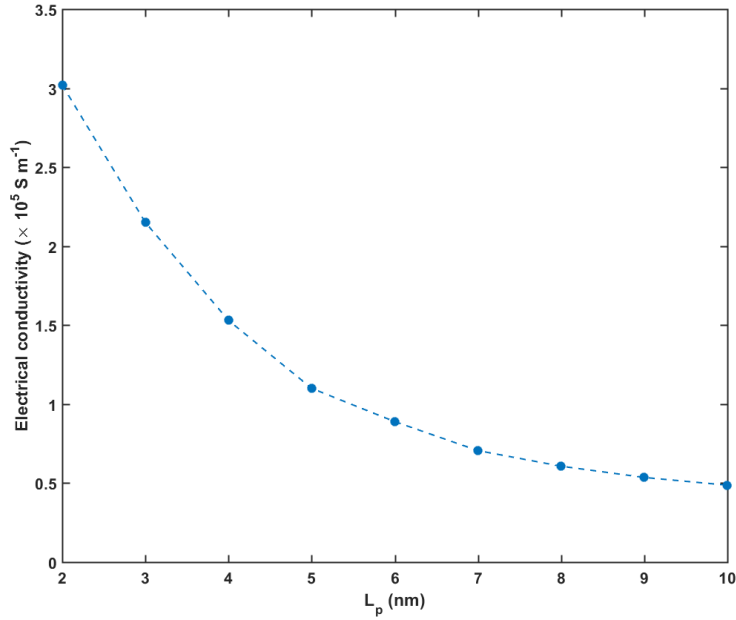
(b) Electrical conductivity reduction due to the increase in period length which restricts electron transport across the barrier.

Figure 4.6: Effect of period length L_p on thermoelectric parameters $N_D = 4 \times 10^{19} \, cm^{-3}$ and $V_0 = 1 \, k_B T$ at $T = 300 \, K$ for silicon.
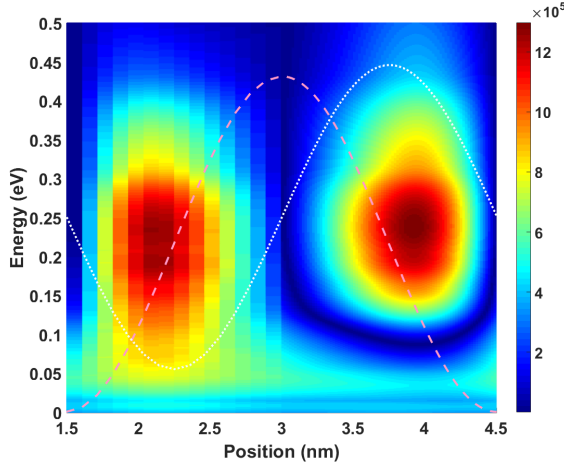
(a) $\sigma(E)$ at $V_0 = 1\,k_B T$ and $L_p = 3 nm$
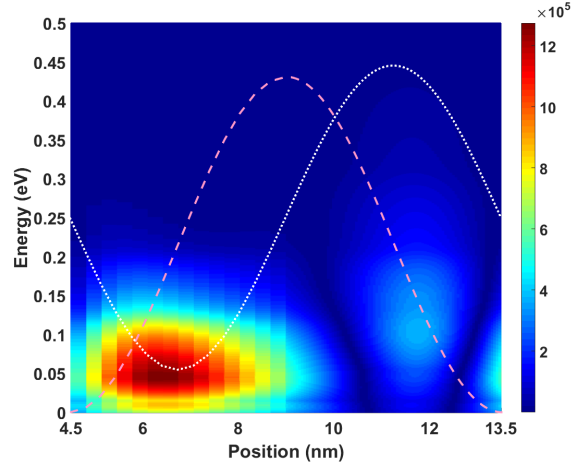
(b) $\sigma(E)$ at $V_0 = 1\,k_B T$ and $L_p = 9\,nm$
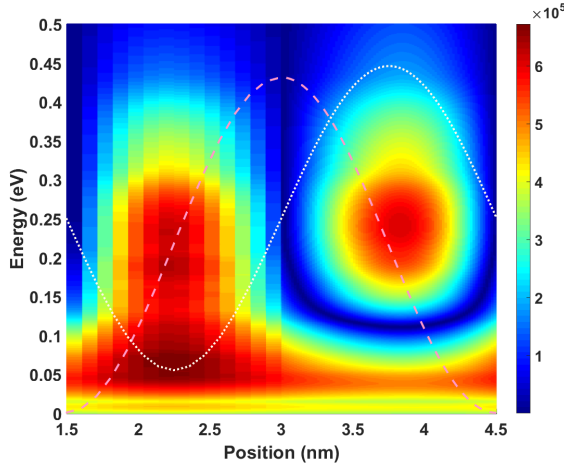
(c) $\sigma(E)$ at $V_0 = 0.4\,k_B T$ and $L_p = 3\,nm$
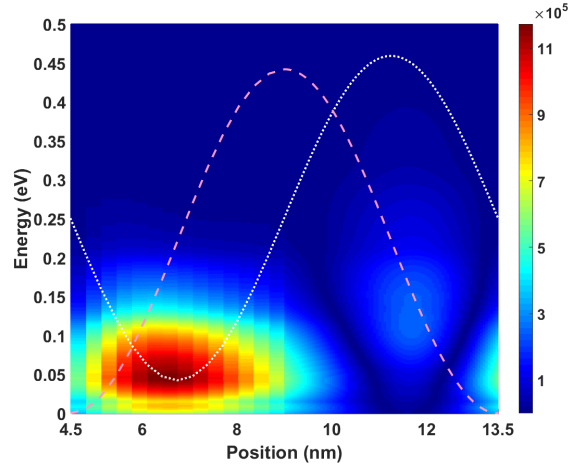
(d) $\sigma(E)$ at $V_0 = 0.4\,k_B T$ and $L_p = 9\,nm$
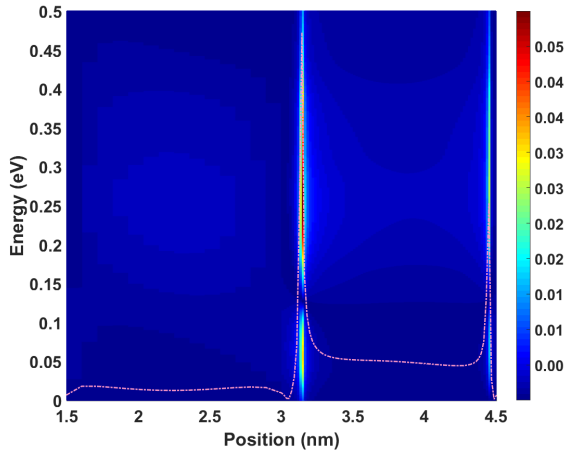
(e) $S(E)$ at $V_0 = 1\,k_B T$ and $L_p = 3\,nm$
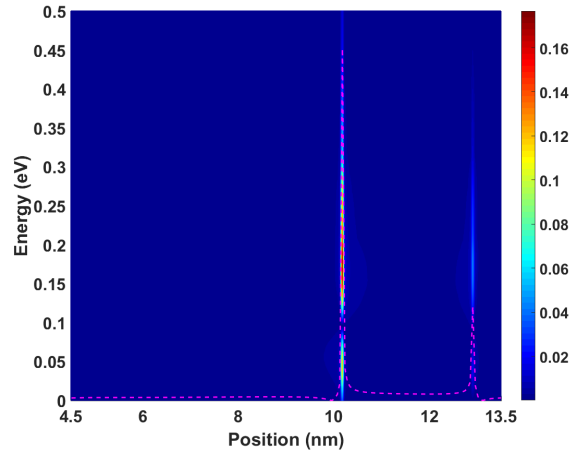
(f) $S(E)$ at $V_0 = 1\,k_B T$ and $L_p = 9\,nm$

Figure 4.7: Energy dependence of Seebeck coefficient (S) and electrical conductivity (σ) with $N_D = 4 \times 10^{19}\,cm^{-3}$ at $T = 300\,K$ for Silicon.

44

contribution from low energy carriers after the barrier decreases as we move from low to high barrier widths due to the restricted tunneling, resulting in lower Seebeck coefficient. Also near this maximum contribution position, $S(E)$ has two peaks which are also reported in [35].

4.5.3.2 Effect of potential barrier height (V_0)

Next, we investigated the influence of barrier height (V_0) on the thermoelectric coefficients. Fig. 4.8 show the variation in Seebeck coefficient and electrical conductivity at a donor concentration of $N_D = 4 \times 10^{19} \, cm^{-3}$ with a different barrier heights. Seebeck coefficient (S) shown in Fig. 4.8a and Fig. 4.8b increases with increase in barrier height as expected, due to the increase in the energy filtering and S depends on the average energy of carriers that participate in transport. This can be seen in Fig. 4.7a and Fig. 4.7c, whereas we increase the V_0 there is an increase in the contribution from high energy electrons i.e electron filtering towards transport even though there tunneling due to thin barriers ($L_p = 3 \, nm$). At wider barrier widths ($L_p = 9 \, nm$), there is an increase in S (Fig. 4.8b) only due to the energy filtering which can be observed in 4.7b and Fig. 4.7d.

Now moving to electrical conductivity (σ), it shows different behavior depending on the barrier width as shown in Fig. 4.8c and Fig. 4.8d. At thin barrier width ($L_p = 3 \, nm$) as seen in Fig. 4.7a and Fig. 4.7c, tunneling dominates so with an increase in the barrier height (V_0) we are making the barrier thinner near its peak which, in turn, facilitates for more tunneling. This results in the increase in electrical conductivity we see in Fig. 4.8c. But at wider barriers ($L_p = 9 \, nm$) there is a combination of energy filtering and tunneling effects that control the conductivity. At short barrier heights, energy filtering plays a major role and restricts more electrons from participating in the transport as we increase the barrier height. But, after that, as we increase the barrier height the effective width of barrier decrease near

(a) S at $L_p = 3\,nm$

(b) S at $L_p = 9\,nm$

(c) σ at $L_p = 3\,nm$

(d) σ at $L_p = 9\,nm$
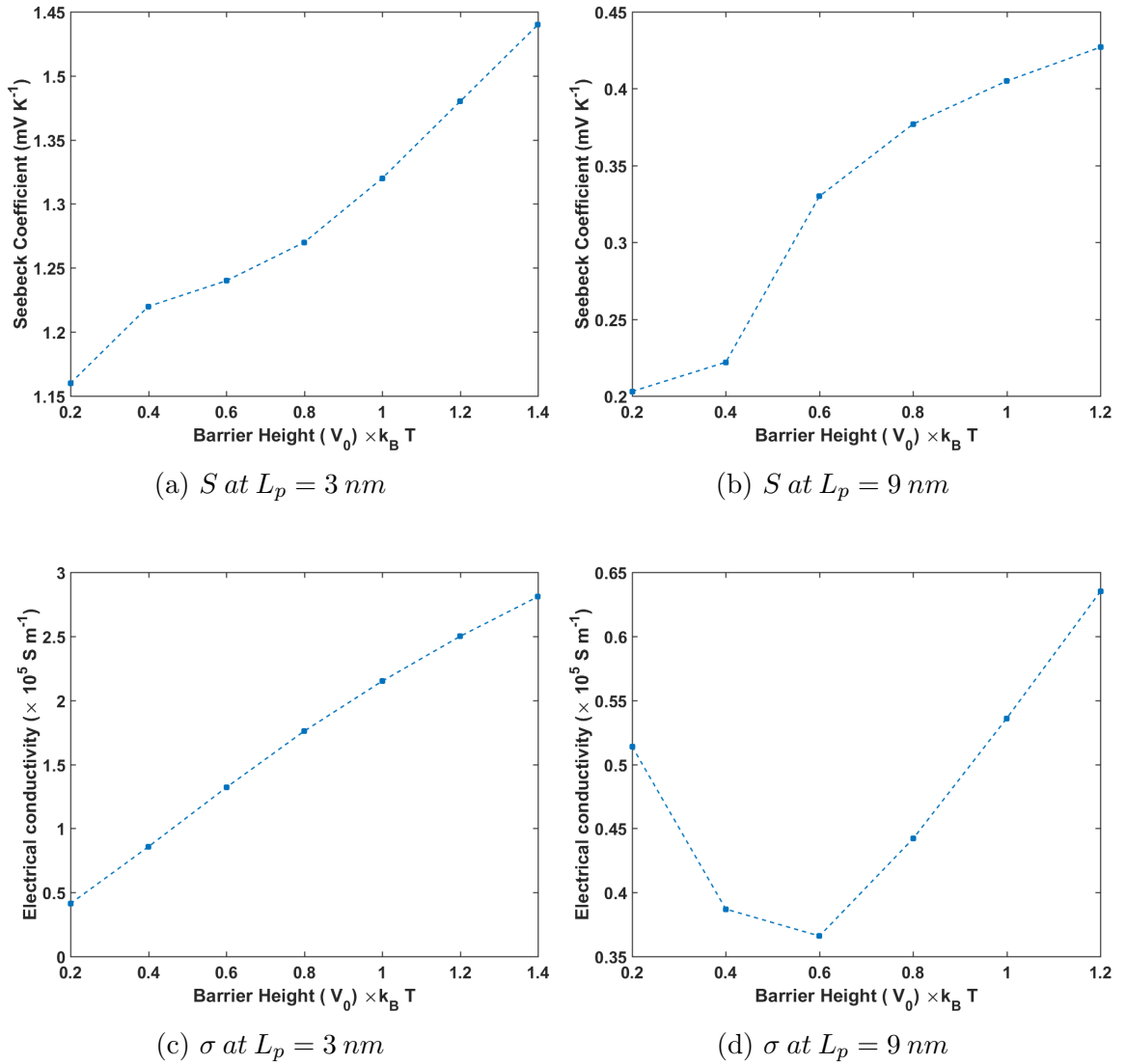
Figure 4.8: Effect of barrier height (V_0) on thermoelectric parameters along with the periodic length to show the interplay between energy filtering and tunneling effects. Here simulation is done with $N_D = 4 \times 10^{19}\,cm^{-3}$ at $T = 300\,K$ for silicon.

its peak facilitating tunneling. This results in an increase in the conductivity from $V_0 = 0.6\,k_B T$ after the initial decrease.

4.5.3.3   Effect of potential barrier smoothness (β)

Till now we have studied the effect of period length and height of a smooth cosine shaped potential barrier, but here we examine the effect of barrier smoothness i.e.,

moving from a sharp square shaped potential to smooth cosine shape. To do that we used the parameter β that control the smoothness of a square potential as shown in Eq. 4.24 and solved for the perturbation in distribution function using the quantum evolution Eq. 4.23. As shown in the Fig. 4.9, Seebeck coefficient increases with
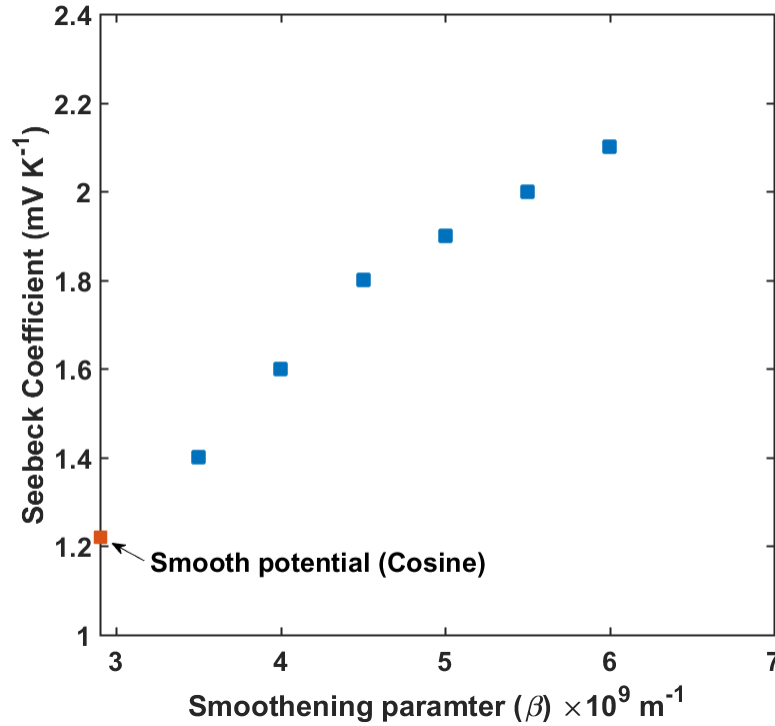
Figure 4.9: Variation in Seebeck coefficient (S) with smoothness of the potential barrier (β) showing the increase in quantum reflections that increase the electron filtering with sharper barriers (higher β).

increase in β i.e., moving to sharper square barriers from smooth ones. This is due to the additional quantum reflections that are introduced in the quantum operator as shown in Eq. 4.23 when compared to the smooth cosine barrier as in Eq. 4.27 which introduces more energy filtering at the barrier. This energy filtering increases with β due to the increase in quantum weight to the quantum evolution which increases the contribution of these quantum reflections.

4.6　Conclusion

Electron filtering is one of the approaches that has been used to improve thermoelectric efficiency. Seebeck coefficient (S) is calculated in Silicon with periodic potentials using the potential operator in Wigner approach. Rode's iterative method is used to calculate the perturbed distribution function (g_i) due to the applied electric field and the quantum evolution due to the rapid varying potentials. Thermoelectric parameters of bulk silicon are calculated to validate the model by comparing it with the literature. Then the confinement or boundary effects are simulated which showed a reduction in conductivity of electrons at low dimensions of silicon and no effect of surface roughness on transport. Then the thermoelectric parameters are calculated for square potential with smoothening and perfectly smooth cosine potential. The effect of tunneling and the energy filtering along with the interplay between them when the potential period and barrier height is changed. Along with that the effect of smoothening is also studied which showed an increase in quantum reflections due to barriers thereby providing more energy filtering. Thus we studied the effect of rapid varying periodic potentials and their shape parameters on thermoelectric parameters in semiconducting nanostructures.

APPENDIX A

SCATTERING RATES

The scattering rates that have been used in our calculations are:

A.1 Acoustic phonon scattering

Acoustic phonon scattering rate (Γ^{3d}_{acs}) in Bulk or 3D material is given as:

$$\Gamma^{3d}_{acs} = \frac{2\pi E^2_{adef} k_B T}{\hbar v^2 \rho} DOS(E) \tag{A.1}$$

Acoustic phonon scattering rate (Γ^{2d}_{acs}) in a 2D material is given as:

$$\Gamma^{2d}_{acs}(\mathbf{k}_x) = \frac{2\pi E^2_{adef} k_B T e^2}{\hbar v^2 \rho} \Xi_{nm} \zeta \tag{A.2}$$

where

$$\Xi_{nm} = \int \int \mid \psi_n(x,y) \mid^2 \mid \psi_m(x,y) \mid^2 dx dy \tag{A.3}$$

$$\zeta = \int \delta(k_x - k'_x + q_x)\delta(E - E')dz \tag{A.4}$$

where E_{adef} is acoustic phonon deformation potential, ρ is density, v is velocity, $DOS(E)$ is density of states and ψ is the electron wave function.

A.2 Intervalley optical phonon scattering

Intervalley optical phonon f-type out-scattering rate (Γ_{iop}^{3d}) in bulk or in a 3D material is given as:

$$\Gamma_{iop}^f = \frac{q(Z-2)D_{kf}^2(N_{po}^f + \frac{1}{2}\pm\frac{1}{2}\pm f_f^\pm)}{\rho\omega_f}DOS(E \pm E_f) \tag{A.5}$$

where E_f is f-type optical phonon energy, f_f is Fermi-Dirac statistics for electron, N_{po}^f is the Bose-Einstein statistics for f-type f-type optical phonons, D_{kf} is f-type optical phonon coupling constant, ω_f is frequency of f-type optical phonons and Z is the number of symmetry directions. '+' denotes absorption of phonon and '-' denotes emission of phonon, the corresponding change in energy of electron are taken care through Fermi-Dirac statistics.

Intervalley optical phonon g-type out-scattering rate (Γ_{iop}^{3d}) in bulk or in a 3D material is given as:

$$\Gamma_{iop}^g = \frac{qD_{kg}^2(N_{po}^g + \frac{1}{2}\pm\frac{1}{2}\pm f_g^\pm)}{\rho\omega_g}DOS(E \pm E_g) \tag{A.6}$$

where E_g is g-type optical phonon energy, f_g is Fermi-dirac statistics for electron, N_{po}^g is the Bose-Einstein statistics for g-type phonon,ω_g is frequency of g-type optical phonons and D_{kg} is g-type optical phonon coupling constant.

Intervalley optical phonon out-scattering rate (Γ_{iop}^{2d}) in 2D material is given as:

$$\Gamma_{iop}^{2d} = \frac{\pi D_{kf|kg}^2}{\rho\omega_{f|g}}(N_{po} + \frac{1}{2}\pm\frac{1}{2})\Xi_{nm}\zeta \tag{A.7}$$

where

$$\Xi_{nm} = \int\int | \psi_n(x,y) |^2| \psi_m(x,y) |^2 \, dxdy \tag{A.8}$$

$$\zeta = \int \delta(k_x - k_x' \pm q_x)\delta(E - E' \pm \hbar\omega_{f|g})dz \tag{A.9}$$

'±' shows that there is both emission and absorption mechanisms corresponding to f-type and g-type optical phonons.

A.3 Deformation potential optical phonon scattering

Deformation potential optical phonon out-scattering rate (Γ_{dop}^{3d}) in Bulk or 3D material is given as:

$$\Gamma_{dop}^{3d} = \frac{\pi D_0^2 (N_{po} + f_{def}^{\pm})}{\rho \omega} DOS(E \pm E_{odef}) \tag{A.10}$$

where D_0 is deformation potential of the optical phonon.

A.4 Impurity scattering

The impurity scattering rate that has been implemented here is derived by Conwell-Weisskopf as

$$\Gamma_{imp} = \frac{Z^2 e^4 N_I}{16\sqrt{2}\pi\epsilon^2 m^{*1/2} E_k^{3/2}} \log\left(1 + \frac{Ze^2 N_I^{1/3}}{4\pi\epsilon E_k}\right) \tag{A.11}$$

where N_I is the number scattering centers created due to the impurities, m^* is effective mass of the material and E_k is the energy of carriers.

A.5 Boundary scattering

The boundary scattering rate where there is confinement of material with width L and velocity of carriers perpendicular to the boundary v_z is given as:

$$\Gamma_{boundary} = \left(\frac{1-p}{1+p}\right)\frac{v}{L} \tag{A.12}$$

where the specularity parameter p is calculated by

$$p = exp(-4k^2\Delta^2 cos(\phi_B)) \tag{A.13}$$

and k is the wave vector of the electron, Δ is the surface roughness and ϕ_B is the angle between the incident electron with the normal of the boundary.

APPENDIX B

DERIVATION OF WIGNER POTENTIAL AND POTENTIAL OPERATOR

B.1   A square potential with smoothening

A periodic fast-varying potential can be written as

$$V_q(r) = \sum_{n=-\infty}^{\infty} V_p(r - nL_p) \tag{B.1}$$

where V_p is the potential and L_p is the period length. The Wigner potential as shown in Eq. 4.5, is

$$V_w(r,k) = \frac{2}{\pi\hbar} \, Im\{e^{2ikr}\hat{V}_q(2k) \sum_{n=-\infty}^{\infty} e^{-2inL_pk}\} \tag{B.2}$$

where $\hat{V}_q(2k)$ is the Fourier transform of V_q and it can be written as

$$V_w(r,k) = \frac{2}{\pi\hbar} Im\{e^{2ikr}\hat{V}_q(2k) \sum_{m=-\infty}^{\infty} \delta(k - m\pi/L_p)\} \tag{B.3}$$

The quantum evolution term (Eq. 4.3)is obtained as

$$Qf_w(r,k) = \frac{2}{\pi\hbar} \sum_{m=-\infty}^{\infty} Im\{e^{2im\pi r/L_p}\hat{V}_q(2m\pi/L_p)\}f_w(r,k - m\pi/L_p)$$

$$= \sum_{m=-\infty}^{\infty} W_m(r)f_w(r,k - m\pi/L_p)$$

$$= \sum_{m=1}^{\infty} W_m(r)\left[f_w(r,k - m\pi/L_p) - f_w(r,k + m\pi/L_p)\right]$$

where the quantum weight $W_m(r)$ is

$$W_m(r) = \frac{2}{\pi\hbar} \sum_{m=-\infty}^{\infty} Im\{e^{2im\pi r/L_p} \hat{V}_q(2m\pi/L_p)\} \tag{B.4}$$

For a periodic potential of period L_p with a square potential of height V_0 with smoothening factor β and width $2a$ of form

$$V_q(r) = \frac{V_0}{2} \{-erf[\beta(r-a)] + erf[\beta(r+a)]\} \tag{B.5}$$

and Fourier transform of $V_q(r)$ is

$$\hat{V}_q(k) = \frac{2V_0}{k} e^{-k^2/(4\beta^2)} sin(ka) \tag{B.6}$$

The quantum weight is obtained as

$$W_m(r) = \frac{2V_0}{\pi\hbar m} e^{\frac{-m^2\pi^2}{\beta^2 L_p^2}} sin\left(\frac{2\pi ma}{L_p}\right) sin\left(\frac{2\pi mr}{L_p}\right) \tag{B.7}$$

B.2 Cosine potential

For a cosine potential of form $V_q(r) = A\,cos(K_0 r)$, the Wigner potential (Eq. 4.5)is obtained as

$$\begin{aligned}
V_w(r,k) &= \frac{2A}{\hbar\pi} Im\{e^{2ikr} \hat{V}_q(2k)\} \\
&= \frac{A}{\hbar\pi} Im\{e^{2ikr} [\delta(2k - K_0) + \delta(2k + K_0)]\} \\
&= \frac{A\,sin(2kr)}{\pi\hbar} [\delta(2k - K_0) + \delta(2k + K_0)]
\end{aligned}$$

54

The potential operator or force term corresponding to potential variation is

$$Qf_w(r,k,t) = \int dk' V_w(r, k - k') f_w(r,k)$$

$$= \int dk' \frac{A \sin(2(k-k')r)}{\pi\hbar} \left[\delta(2(k-k') - K_0) + \delta(2(k-k') + K_0)\right] f_w(r,k)$$

$$= \frac{A \sin(K_0 r)}{\pi\hbar} \left[f_w\left(r, k - \frac{K_0}{2}\right) - f_w\left(r, k + \frac{K_0}{2}\right) \right]$$

BIBLIOGRAPHY

[1] Aksamija, Z., and Knezevic, I. Anisotropy and boundary scattering in the lattice thermal conductivity of silicon nanomembranes. *Phys. Rev. B 82* (2010), 045319.

[2] Aksamija, Z., and Knezevic, I. Thermoelectric properties of silicon nanostructures. *J. Comput. Electron. 9* (2010), 173.

[3] Aksamija, Z., and Knezevic, I. Anisotropy and edge roughness scattering in the lattice thermal conductivity of graphene nanoribbons. *ECS Transactions 35* (2011), 195.

[4] Aksamija, Z., and Knezevic, I. Lattice thermal transport in large-scale polycrystalline graphene. *Phys. Rev. B 90* (2014), 035419.

[5] Ando, T., Fowler, A. B., and Stern, F. Electronic properties of two-dimensional systems. *Rev. Mod. Phys. 54* (1982), 437.

[6] Ashcroft, N. W., and Mermin, N. D. *Solid State Physics.* Brooks/Cole, Belmont, CA, 1976.

[7] Bian, Z., and Shakouri, A. *Monte Carlo Simulation of Solid-State Thermionic Energy Conversion Devices Based on Non-Planar Heterostructure Interfaces.* Springer Berlin Heidelberg, Berlin, Heidelberg, 2006, pp. 179–182.

[8] Boukai, A. I., Bunimovich, Y., Tahir-Kheli, J., Yu, J., III, W. A. Goddard, and Heath, J. R. Silicon nanowires as efficient thermoelectric materials. *Nature 451* (2008), 168.

[9] Chen, R., Hochbaum, A. I., Murphy, P., Moore, J., Yang, P., and Majumdar, A. Thermal conductance of thin silicon nanowires. *Phys. Rev. Lett. 101* (2008), 105501.

[10] Chindalore, G., Hareland, S.A., Jallepalli, S.A., Tasch, A.F., Maziar, C.M., Chia, V.K.F., and Smith, S. Experimental determination of threshold voltage shifts due to quantum mechanical effects in mos electron and hole inversion layers. *Electron Device Letters, IEEE 18*, 5 (May 1997), 206–208.

[11] Chowdhury, I., Prasher, R., Lofgreen, K., Chrysler, G., Narasimhan, S., Mahajan, R., Koester, D., Alley, R., and Venkatasubramanian, R. On-chip cooling by superlattice-based thin-film thermoelectrics. *Nature Nano. 4* (2009), 235–238.

[12] Dragoman, D., and Dragoman, M. Giant thermoelectric effect in graphene. *Appl. Phys. Lett. 91*, 20 (2007), 203116.

[13] Fehlner, W.R., and Loly, P.D. Save: A general approach for calculating the spectral properties of solids. *Solid State Communications 15*, 1 (1974), 69 – 72.

[14] Fischetti, M. V., and Laux, S. E. Monte carlo study of electron transport in silicon inversion layers. *Phys. Rev. B 48* (Jul 1993), 2244–2274.

[15] Fischetti, M. V., Ren, Z., Solomon, P. M., Yang, M., and Rim, K. Six-band **k · p** calculation of the hole mobility in silicon inversion layers: Dependence on surface orientation, strain, and silicon thickness. *J. Appl. Phys. 94*, 2 (2003), 1079–1095.

[16] Geballe, T. H., and Hull, G. W. Seebeck effect in silicon. *Phys. Rev. 98* (May 1955), 940–947.

[17] Goldsmid, H.J. *Electronic refrigeration.* Pion, London, UK, 1986.

[18] Granacher, I., and Czaja, W. Mobility and electron spin resonance linewidth in phosphorus doped silicon. *Journal of Physics and Chemistry of Solids 28*, 2 (1967), 231 – 238.

[19] Hicks, L.D., and Dresselhaus, M.S. Effect of quantum-well structures on the thermoelectric figure of merit. *Phys. Rev. B 47* (1993), 12727.

[20] Hicks, L.D., and Dresselhaus, M.S. Thermoelectric figure of merit of a one-dimensional conductor. *Phys. Rev. B 47* (1993), 16631.

[21] Hochbaum, A.I., Chen, R., Delgado, R.D., Liang, W., Garnett, E.C., Najarian, M., Majumdar, A., and Yang, P. Enhanced thermoelectric performance of rough silicon nanowires. *Nature 451* (2008), 163.

[22] Huang, Minghuang, Ritz, Clark S., Novakovic, Bozidar, Yu, Decai, Zhang, Yu, Flack, Frank, Savage, Donald E., Evans, Paul G., Knezevic, Irena, Liu, Feng, and Lagally, Max G. Mechano-electronic superlattices in silicon nanoribbons. *ACS Nano 3* (2009), 721–727.

[23] Jacoboni, C., and Reggiani, L. The monte-carlo method for the solution of charge transport in semiconductors with applications to covalent materials. *Rev. Mod. Phys. 55* (1983), 645.

[24] Kim, R., Datta, S., and Lundstrom, M. S. Influence of dimensionality on thermoelectric device performance. *J. Appl. Phys. 105*, 3 (2009), 034506.

[25] Kim, R., and Lundstrom, M. S. Computational study of the seebeck coefficient of one-dimensional composite nano-structures. *J. Appl. Phys. 110* (2011), 034511.

[26] Knezevic, I., Ramayya, E. B., Vasileska, D., and Goodnick, S. M. Diffusive transport in quasi-2d and quasi-1d electron systems. *J. Comput. Theor. Nanosci. 6*, 8 (2009), 1725–1753.

[27] Mahan, G D, and Sofo, J O. The best thermoelectric. *Proc. Natl. Acad. Sci. U. S. A. 93* (1996), 7436–7439.

[28] Mahan, G D, and Sofo, J O. The best thermoelectric. *Proceedings of the National Academy of Sciences 93*, 15 (1996), 7436–7439.

[29] Mahan, G. D., and Woods, L. M. Multilayer thermionic refrigeration. *Phys. Rev. Lett. 80* (1998), 4016–4019.

[30] Majumdar, A. Thermoelectric devices: Helping chips to keep their cool. *Nature Nano. 4* (2009), 214–215.

[31] Markussen, T., Jauho, A.-P., and Brandbyge, M. Surface-decorated silicon nanowires: A route to high-ZT thermoelectrics. *Phys. Rev. Lett. 103* (2009), 055502.

[32] Morelli, D. T., Heremans, J. P., and Slack, G. A. Estimation of the isotope effect on the lattice thermal conductivity of group IV and group III-V semiconductors. *Phys. Rev. B 66*, 19 (2002), 195304.

[33] Nakpathomkun, Natthapon, Xu, H. Q., and Linke, Heiner. Thermoelectric efficiency at maximum power in low-dimensional systems. *Phys. Rev. B 82* (Dec 2010), 235428.

[34] Nedjalkov, M., Querlioz, D., Dollfus, P., and Kosina, H. Wigner function approach. In *Nano-Electronic Devices*, Dragica Vasileska and Stephen M. Goodnick, Eds. Springer New York, 2011, pp. 289–358.

[35] Neophytou, N.and Kosina, H. Optimizing thermoelectric power factor by means of a potential barrier. *Journal of Applied Physics 114*, 4 (2013).

[36] Neophytou, N., and Thesberg, M. Modulation doping and energy filtering as effective ways to improve the thermoelectric power factor. *Journal of Computational Electronics 15*, 1 (2016), 16–26.

[37] Neophytou, N., Zianni, X., Kosina, H., Frabboni, S., Lorenzi, B.o, and Narducci, D. Simultaneous increase in electrical conductivity and seebeck coefficient in highly boron-doped nanocrystalline si. *Nanotechnology 24*, 20 (2013), 205402.

[38] Patrick, W.J. Measurement of resistivity and mobility in silicon epitaxial layers on a control wafer. *Solid-State Electronics 9*, 3 (1966), 203 – 211.

[39] Ramayya, E. B., Maurer, L. N., Davoody, A. H., and Knezevic, I. Thermoelectric properties of ultrathin silicon nanowires. *Phys. Rev. B 86* (2012), 115328.

[40] Ramayya, E. B., Vasileska, D., Goodnick, S. M., and Knezevic, I. Electron transport in silicon nanowires: the role of acoustic phonon confinement and surface roughness scattering. *J. Appl. Phys. 104* (2008), 063711.

[41] Ridley, B. K. *Quantum Processes in Semiconductors.* Oxford Science Publications, 2000.

[42] Rode, D. L. Electron transport in insb, inas, and inp. *Phys. Rev. B 3* (1971), 3287–3299.

[43] Ryu, H. J., Aksamija, Z., Paskiewicz, D. M., Scott, S. A., Lagally, M. G., Knezevic, I., and Eriksson, M. A. Quantitative determination of contributions to the thermoelectric power factor in si nanostructures. *Phys. Rev. Lett. 105* (2010), 256601.

[44] Shakouri, Ali. Recent developments in semiconductor thermoelectric physics and materials. *Annu. Rev. Mater. Res. 41*, 1 (2011), 399–431.

[45] Shi, Li. Thermal and thermoelectric transport in nanostructures and low-dimensional systems. *Nanoscale and Microscale Thermophysical Engineering 16*, 2 (2012), 79–116.

[46] Wigner, E. On the quantum correction for thermodynamic equilibrium. *Phys. Rev. 40* (Jun 1932), 749–759.

[47] Wu, C.-Y., Banerjee, S., Sadra, K., Streetman, B.G., and Sivan, R. Quantization effects in inversion layers of pmosfets on si (100) substrates. *Electron Device Letters, IEEE 17*, 6 (June 1996), 276–278.

[48] Yasaei, P., Fathizadeh, A., Hantehzadeh, R., Majee, A. K., El-Ghandour, A., Estrada, D., Foster, C., Aksamija, Z., Khalili-Araghi, F., and Salehi-Khojin, A. Bimodal phonon scattering in graphene grain boundaries. *Nano Letters 15*, 7 (2015), 4532–4540.

[49] Yokomizo, Y., and Nakamura, J. Giant seebeck coefficient of the graphene/h-bn superlattices. *Appl. Phys. Lett. 103*, 11 (2013), 113901.

[50] Zhou, J., Yang, R., Chen, G., and Dresselhaus, M. S. Optimal bandwidth for high efficiency thermoelectrics. *Phys. Rev. Lett. 107* (2011), 226601.

[51] Zhou, Jun, Yang, Ronggui, Chen, Gang, and Dresselhaus, Mildred S. Optimal bandwidth for high efficiency thermoelectrics. *Phys. Rev. Lett. 107* (2011), 226601.

[52] Zide, J. M. O., Bahk, J.-H., Singh, R., Zebarjadi, M., Zeng, G., Lu, H., Feser, J. P., Xu, D., Singer, S. L., Bian, Z. X., Majumdar, A., Bowers, J. E., Shakouri, A., and Gossard, A. C. High efficiency semimetal/semiconductor nanocomposite thermoelectric materials. *J. Appl. Phys. 108*, 12 (2010), 123702.

[53] Ziman, J. *Electrons and Phonons: The Theory of Transport Phenomena in Solids.* Oxford University Press Inc., 1960.